

DEFT: Differentiable Branched Discrete Elastic Rods for Modeling Furcated DLOs in Real-Time

Yizhou Chen Xiaoyue Wu Yeheng Zong Yuzhen Chen Anran Li
Bohao Zhang Ram Vasudevan

Department of Robotics, University of Michigan, Ann Arbor, MI 48109, United States
{yizhouch, wxyluna, yehengz, yuzhenc, anranli, jimzhang, ramv}@umich.edu
<https://roahmlab.github.io/DEFT/>

Abstract: Autonomous wire harness assembly requires robots to manipulate complex branched cables with high precision and reliability. A key challenge in automating this process is accurately predicting how flexible branched structures behave during manipulation. Without accurate predictions, robots cannot reliably execute assembly operations. While existing research has made progress in modeling single-threaded Deformable Linear Objects (DLOs), extending these approaches to Branched Deformable Linear Objects (BDLOs) presents fundamental challenges. The junction points in BDLOs create complex force interactions and strain propagation patterns that cannot be adequately captured by simply connecting multiple single-DLO models. To address these challenges, this paper introduces Differentiable discrete branched Elastic rods for modeling Furcated DLOs in real-Time (DEFT), a novel framework that combines a differentiable physics-based model with a learning framework to: 1) accurately model BDLO dynamics, including dynamic propagation at junction points and grasping in the middle of a BDLO, 2) achieve efficient computation for real-time inference, and 3) enable planning to demonstrate dexterous BDLO manipulation. A comprehensive series of real-world experiments demonstrate that DEFT outperforms state-of-the-art methods in accuracy, computational speed, and planning success rate.

Keywords: Branched Deformable Linear Objects Modeling, Physics-Informed Learning, Differentiable Simulation

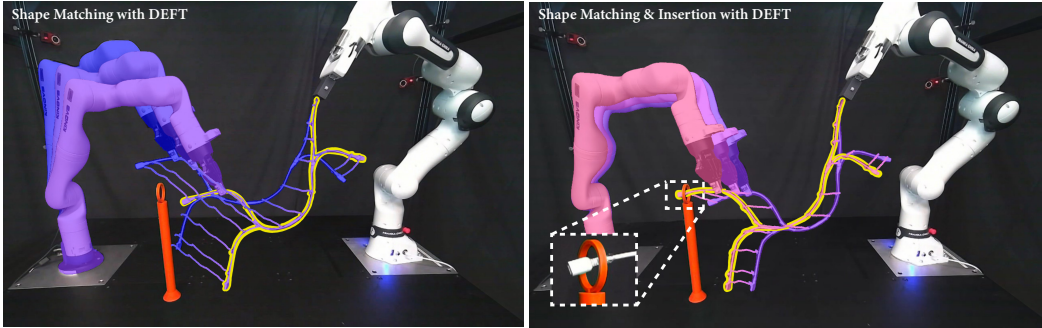


Figure 1: As this paper illustrates, DEFT can be used in concert with a motion planning algorithm to autonomously manipulate BDLOs. The figures above illustrate how DEFT can be used to autonomously complete a wire insertion task. **Left:** The system first plans a shape-matching motion, transitioning the BDLO from its initial configuration to the target shape (contoured with yellow), which serves as an intermediate waypoint. **Right:** Starting from the intermediate configuration, the system performs thread insertion, guiding the BDLO into the target hole while also matching the target shape. Notably, DEFT predicts the state of the wire recursively without relying on ground truth or perception data at any point in the process.

1 Introduction

The automation of wire harness assembly represents a critical challenge in manufacturing, particularly in the automotive and aerospace industries where complex, branched cable systems are essential components. These assemblies require robots to manipulate Branched Deformable Linear Objects (BDLOs) with precision over extended periods ($\geq 5s$) [1–3], a task that remains largely unautomated due to the objects’ complex nonlinear dynamics. Further complicating matters, practical assembly environments often involve occlusions, limiting perception systems’ ability to estimate full BDLO configurations reliably [4]. Thus, robust assembly requires accurate BDLO models for reliable long-term open-loop predictions. While accurate prediction of BDLO behavior is possible through computationally intensive models, real-time manipulation demands rapid computation.

Deep neural networks (DNNs) for tree-structured data [5–8] can achieve real-time prediction performance for BDLOs but often require large datasets and lack robustness to variations in BDLOs. A promising alternative combines differentiable physics models as high-fidelity priors with DNNs to improve sample efficiency and generalizability [9–15]. However, this approach has not yet been applied to BDLO dynamics due to two significant challenges: First, the field lacks an accurate, efficient, differentiable physics model for BDLOs. Current models compromise speed for accuracy and do not preserve gradients needed for parameter optimization. Second, to the best of our knowledge, there is no existing research demonstrating that DNNs can effectively learn residual dynamics specifically for BDLOs.

To address these challenges, this paper introduces **Differentiable Branched Discrete Elastic Rods for Modeling Furcated DLOs in Real-Time (DEFT)**, a novel differentiable physics-based framework that accurately predicts dynamic BDLO behavior over long time horizons with real-time inference capabilities. The contributions of this paper are four-fold: First, a novel differentiable BDLO model that accurately captures dynamics propagation at junctions, enabling efficient parameter identification. Second, a computational representation that enables efficient inference and model parameter learning through parallel programming combined with analytical gradients. Third, a specialized Graph Neural Network (GNN) architecture for residual learning to correct numerical integration errors over long horizons. Fourth, a comprehensive experimental validation demonstrating that DEFT outperforms prior methods in accuracy, speed, and sample efficiency while enabling practical applications such as 3-D shape matching, multi-branch grasping, and thread insertion (Figure 1). The framework is implemented in PyTorch for seamless integration with deep learning workflows, and represents, to the best of our knowledge, the first quantitative study of BDLO modeling and manipulation in real-world settings. A visualization of DEFT’s contributions can be found in Appendix B.1.

2 Related Work

Physics-Based Modeling. Several methods adapt tree or cloth modeling to branched structures. FEM-based approaches [16–22] offer high 3D accuracy but require extensive parameter tuning and are computationally intensive. Discrete Elastic Rods (DER) [23, 24] model branches individually using elastic rod theory with rigid-body constraints at junction points. These methods are reasonably accurate, but rely on fixed parameters that limit learning and require precise orientation tracking, which is impractical for robotic tasks. Quasi-static methods like ASMC [25] prioritize speed by enforcing geometric constraints, which can make parameter identification difficult and compromise dynamic fidelity.

Learning-Based Modeling. Unlike physics-based approaches, neural networks learn from real-world data. While Tree-LSTM [5, 26] and Graph Neural Networks (GNNs) [6–8] can process vertex-level spatial information for BDLOs, our experiments show they struggle to accurately capture complex 3D dynamic deformations during actual manipulation tasks.

Physics-Learning Hybrid Modeling. Recent research combines physics-based modeling with learning [10–15]. For instance, DEFORM [14] focuses on modeling single-threaded DLOs using a differentiable DER (DDER) model and residual learning to correct numerical integration errors.

However, DEFORM lacks fundamental capabilities essential for accurate and efficient BDLO modeling. Our experiments show that extending DEFORM to BDLOs reduces computational efficiency and fails to capture branching point dynamics, leading to inaccurate predictions. DEFT addresses these limitations by adapting DDER for individual branches and introduces several novel contributions (as described in the Introduction) for accurate, efficient BDLO simulation. Comprehensive ablation studies and comparisons validate DEFT’s advantages over DEFORM extensions and state-of-the-art methods.

3 Preliminaries

Deformable Linear Object (DLO) Model. We represent a DLO as an indexed set of n vertices at each time instance. The ground truth location of vertex i at time t is denoted by $\mathbf{x}_t^i \in \mathbb{R}^3$, and the set of all n vertices is denoted by \mathbf{X}_t . A segment, or edge, in the DLO is the line between successive vertices, $\mathbf{e}_t^i = \mathbf{x}_t^{i+1} - \mathbf{x}_t^i$. Let \mathbf{E}_t correspond to the set of all edges at time t . Let $\mathbf{M}_i \in \mathbb{R}^{3 \times 3}$ denote the mass matrix of vertex i . The velocity of the vertices of the DLO is approximated by $\mathbf{V}_t = (\mathbf{X}_t - \mathbf{X}_{t-1})/\Delta t$, where Δt is the time step between frames. Note that \mathbf{V}_t is an approximation of the actual velocities. We distinguish between ground truth elements and predicted elements by using the circumflex symbol (e.g., \mathbf{X}_t is the ground truth set of vertices at time t , and $\hat{\mathbf{X}}_t$ is the predicted set of vertices at time t).

Differentiable Discrete Elastic Rods (DDER). DDER builds upon DER theory to model three distinct deformation modes of DLOs: bending, twisting, and stretching while being able to auto-tune model parameters from real-world dataset. We briefly summarize DER in this section. A longer introduction can be found in Appendix A). To predict $\hat{\mathbf{X}}_{t+1}$, DER assigns a scalar angle $\theta_t^i \in \mathbb{R}$ to each segment and uses these angles to construct $n - 1$ material frames at time t , denoted by $\Gamma(\mathbf{X}_t, \boldsymbol{\theta}_t)$. Let $\boldsymbol{\alpha}$ represent the vector of material properties for each vertex of the DLO (i.e., mass, bending modulus, and twisting modulus) [23, §4.2]. Using these definitions, one can compute the potential energy of the DLO arising from bending and twisting, which we denote by $P(\Gamma(\mathbf{X}_t, \boldsymbol{\theta}_t), \boldsymbol{\alpha})$. At each step, DER assumes quasi-static equilibrium, calculates the optimal angles $\boldsymbol{\theta}_t^*$ by minimizing $P(\Gamma(\mathbf{X}_t, \boldsymbol{\theta}_t), \boldsymbol{\alpha})$ with respect to the decision variables $\boldsymbol{\theta}_t$. Once $\boldsymbol{\theta}_t^*(\mathbf{X}_t, \boldsymbol{\alpha})$ is derived, the restorative force during deformation is given by the negative gradient of the potential energy with respect to the vertices. Consequently, the equation of motion for the DLO is:

$$\mathbf{M}\ddot{\mathbf{X}}_t = - \frac{\partial P(\Gamma(\mathbf{X}_t, \boldsymbol{\theta}_t^*(\mathbf{X}_t, \boldsymbol{\alpha})), \boldsymbol{\alpha})}{\partial \mathbf{X}_t} \quad (1)$$

One can numerically integrate this formula to predict the velocity and position $\hat{\mathbf{X}}_{t+1}$ by applying the Semi-Implicit Euler method. Consequently, minimizing the prediction loss requires solving a bi-level optimization problem at each time step t :

$$\min_{\boldsymbol{\alpha}} \|\mathbf{X}_{t+1} - \hat{\mathbf{X}}_{t+1}(\boldsymbol{\theta}_t^*)\|_2 \quad (2)$$

$$\boldsymbol{\theta}_t^* = \arg \min_{\boldsymbol{\theta}_t} P(\Gamma(\mathbf{X}_t, \boldsymbol{\theta}_t), \boldsymbol{\alpha}) \quad (3)$$

Note $\hat{\mathbf{X}}_{t+1}$ depends on the previously computed $\boldsymbol{\theta}_t^*$ through (3). To compute the gradient of (3) with respect to $\boldsymbol{\alpha}$, DDER employs solvers from Theseus [27], which use PyTorch’s automatic differentiation [28]. As we illustrate via experiments in §5, this can be a time-consuming process.

4 Methodology

4.1 Branched Deformable Linear Object (BDLO) Model

We model a BDLO by decomposing its structure into a hierarchy of DLOs. The parent DLO is defined as the minimum-length path through the BDLO that connects the two end-effectors (i.e., the points where the structure is manipulated or anchored). All other branches diverging from this primary path are modeled as children DLOs that maintain their physical connection to the parent

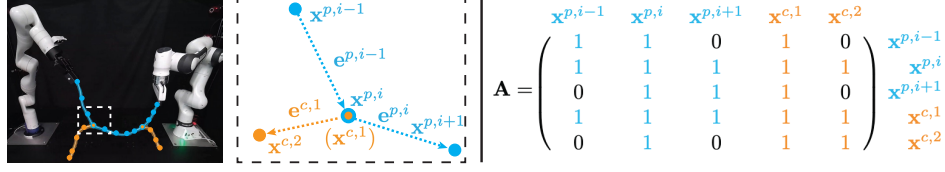


Figure 2: **Left:** An example configuration of BDLO manipulation, relevant notation and structure at a junction. **Right:** The adjacency matrix \mathbf{A} for the junction in left captures both self-loops (diagonal entries) and inter-node connections (off-diagonal entries). By embedding each node’s local dynamics alongside its coupling to neighboring nodes, \mathbf{A} enables an graph representation of the BDLO’s behavior.

DLO at their attachment points, which we refer to as *junction points*. The parent and children DLOs are each modeled as DLOs using DDER and inherit all previously introduced notation. Denote the parent and child DLOs using superscripts p and c , respectively. At a junction located at vertex i , associated edges are $\mathbf{e}_t^{p,i-1}$, $\mathbf{e}_t^{p,i}$, and $\mathbf{e}_t^{c,1}$ as shown in Figure 2 (left). To capture bending and twisting effects at the junction, we introduce the moment of inertia $\mathbf{I}^i \in \mathbb{R}^{3 \times 3}$ for the i -th edge, representing mass distribution resistance to rotation. Edge orientation is described by an angle-axis vector $\boldsymbol{\Omega}_t^i \in \mathbb{R}^3$, defined in Appendix B.2. The orientation and position of the two end effectors at time t are denoted by $\mathbf{u}_t \in \mathbb{R}^{12}$. \mathbf{u}_t is referred to as the input.

4.2 DEFT Overview

At each time t , DEFT simulates the behavior of a BDLO when given predictions of the vertices and their velocities under a specified input as described in Algorithm 1. It begins by first associating the grasped vertices with the robot end effector inputs \mathbf{u}_t . DEFT then computes their respective material frames, which are subsequently used to calculate each branch’s potential energy (Line 2). DEFT then minimizes this potential energy using analytical gradients to determine the optimal parameters $\boldsymbol{\theta}_t^*$ and updates the potential energy accordingly (Line 3). These forces are integrated forward in time using a Semi-Implicit Euler method combined with residual learning to update the vertex velocities and positions (Lines 4 and 5). To further accelerate above computation, DEFT processes the parent and child DLOs in parallel.

Algorithm 1 $(\hat{\mathbf{X}}_{t+1}, \hat{\mathbf{V}}_{t+1}) = \text{DEFT}(\hat{\mathbf{X}}_t, \hat{\mathbf{V}}_t, \mathbf{u}_t)$

- 1: Associate grasped vertices with \mathbf{u}_t
- 2: Calculate Material Frames $\Gamma(\mathbf{X}_t, \boldsymbol{\theta}_t)$
- 3: $\boldsymbol{\theta}_t^*(\mathbf{X}_t, \boldsymbol{\alpha}) = \arg \min_{\boldsymbol{\theta}_t} P(\Gamma(\mathbf{X}_t, \boldsymbol{\theta}_t), \boldsymbol{\alpha})$ \triangleright §4.5
- 4: $\hat{\mathbf{V}}_{t+1} = \hat{\mathbf{V}}_t - \Delta_t \mathbf{M}^{-1} \frac{\partial P(\Gamma(\mathbf{X}_t, \boldsymbol{\theta}_t^*(\mathbf{X}_t, \boldsymbol{\alpha})), \boldsymbol{\alpha})}{\partial \mathbf{X}_t}$ \triangleright (1)
- 5: $\hat{\mathbf{X}}_{t+1} = \hat{\mathbf{X}}_t + \Delta_t \hat{\mathbf{V}}_{t+1} + \text{GNN}$ \triangleright §4.3
- 6: Constraints enforcement on $\hat{\mathbf{X}}_{t+1}$ \triangleright §4.4
- 7: $\hat{\mathbf{V}}_{t+1} = (\hat{\mathbf{X}}_{t+1} - \hat{\mathbf{X}}_t) / \Delta_t$ \triangleright Velocity Update

return $\hat{\mathbf{X}}_{t+1}, \hat{\mathbf{V}}_{t+1}$

Numerical integration errors can cause unintended changes in branch lengths. Additionally, DEFT initially treats each branch’s internal dynamics independently, ignoring junction interactions, which can impede the propagation of dynamics, such as bending and twisting, across junctions or even cause branch detachment. To overcome this, DEFT enforces constraints ensuring branch inextensibility, junction connectivity, and proper propagation of deformation effects (Line 6). Applying Algorithm 1 iteratively enables accurate BDLO state predictions over extended time horizons. An algorithm overview is illustrated in Appendix B.1.

4.3 Integration Method with Residual Learning

This subsection constructs the GNN for residual learning in integration method. We employ a GNN to represent BDLOs as graphs where vertices become nodes and edges capture both intra-branch connections and junctions. This graph-based formulation translates into an adjacency matrix $\mathbf{A} \in \mathbb{R}^{(n^p + n^c) \times (n^p + n^c)}$, which links individual branch nodes and explicitly encodes node information across branch junctions. This adjacency matrix is defined as follows: the entry \mathbf{A}_{i_1, i_2} equals 1 if there’s an edge between vertices i_1 and i_2 , and 0 otherwise. Figure 2 depicts an example \mathbf{A} . This adjacency matrix is utilized within a Graph Convolutional Network (GCN) [8] to aggregate learned

features. A single GCN layer is defined as

$$\text{GCN}(\hat{\mathbf{X}}_t, \hat{\mathbf{V}}_t, \alpha) = \tilde{\mathbf{A}} \mathbf{F}_t(\hat{\mathbf{X}}_t, \hat{\mathbf{V}}_t, \alpha) \mathbf{W}, \quad \tilde{\mathbf{A}} = \mathbf{D}^{-\frac{1}{2}} \mathbf{A} \mathbf{D}^{-\frac{1}{2}}, \quad (4)$$

where $\tilde{\mathbf{A}}$ is the normalized adjacency matrix. Note that $\tilde{\mathbf{A}}$ is the normalization of \mathbf{A} using the degree matrix $\mathbf{D} = \text{diag}(d_1, d_2, \dots, d_n)$ where $d_{i1} = \sum_{i2} A_{i1,i2}$. This normalization ensures nodes with higher degrees do not disproportionately influence the model, maintaining consistent feature magnitudes across representations [29]. The details node feature matrix, $\mathbf{F}_t(\hat{\mathbf{X}}_t, \hat{\mathbf{V}}_t, \alpha) \in \mathbb{R}^{(n^p+n^c) \times h}$ and the trainable weight matrix $\mathbf{W} \in \mathbb{R}^{h \times 3}$ can be found in Appendix B.3.

4.4 Enforcing Constraints

After numerical integration, DEFT applies constraints to maintain branch inextensibility, junction attachment, and enable deformation propagation by updating vertex positions using correction terms. Direct projection onto constraint sets may cause nonlinear momentum changes, and can lead to simulation instability and inaccurate system identification. Alternatively, inspired by the PBD method [30], DEFT computes correction terms via optimization to preserve momentum, resulting in stable and realistic simulations. Below, we introduce a theorem that can be applied to enforce inextensibility, attachment at the junctions, and deformation propagation. Note that we omit the time subscript t in the statement of the theorem for simplicity.

Theorem 1. *Consider two consecutive bodies a and b , represented by adjacent vertices or edges, that are subject to a holonomic constraint $C(\hat{\mathbf{z}}) = 0$, where $\hat{\mathbf{z}} = [\hat{\mathbf{x}}^a, \hat{\mathbf{x}}^b, \hat{\boldsymbol{\Omega}}^a, \hat{\boldsymbol{\Omega}}^b]$. Suppose $\hat{\mathbf{z}}$ does not satisfy the holonomic constraint and one calculates a correction $\Delta\hat{\mathbf{z}}$ to $\hat{\mathbf{z}}$ to satisfy the holonomic constraint by solving the following momentum constrained optimization problem.*

$$\min_{\Delta\hat{\mathbf{z}}} \frac{1}{2} C(\hat{\mathbf{z}} + \Delta\hat{\mathbf{z}})^2, \quad (5)$$

$$\text{s.t.} \quad \mathbf{M}^a \Delta\hat{\mathbf{x}}^a + \mathbf{M}^b \Delta\hat{\mathbf{x}}^b = 0, \quad (6)$$

$$\mathbf{I}^a \Delta\hat{\boldsymbol{\Omega}}^a + \mathbf{I}^b \Delta\hat{\boldsymbol{\Omega}}^b = 0. \quad (7)$$

If C is affine, differentiable, and symmetric in $\Delta\hat{\mathbf{z}}$, then when Δ_t is sufficiently small there exists an analytical formula for the unique solution to the optimization problem.

The proof of this theorem for each of the relevant constraints and the formula for the optimal solution can be found in Appendix B.4. We next demonstrate how this theorem can be applied to enforce inextensibility, junction attachment, and deformation propagation. To enforce inextensibility, let $\bar{\mathbf{e}}_i$ denote the undeformed edge between vertices $\hat{\mathbf{x}}^i$ and $\hat{\mathbf{x}}^{i+1}$. Set $\hat{\mathbf{z}}_I = [\hat{\mathbf{x}}^i, \hat{\mathbf{x}}^{i+1}, \hat{\boldsymbol{\Omega}}^i, \hat{\boldsymbol{\Omega}}^{i+1}]$, $C_I(\hat{\mathbf{z}} + \Delta\hat{\mathbf{z}}) = \|(\hat{\mathbf{x}}^i + \Delta\hat{\mathbf{x}}^i) - (\hat{\mathbf{x}}^{i+1} + \Delta\hat{\mathbf{x}}^{i+1})\|_2 - \|\bar{\mathbf{e}}_i\|_2$ so that the updated edge length is equal to its undeformed length. To enforce attachment at the junction, define $\hat{\mathbf{z}}$ and $g(\hat{\mathbf{z}} + \Delta\hat{\mathbf{z}})$ between parent-branch vertex $\hat{\mathbf{x}}^{p,i}$ and child-branch vertex $\hat{\mathbf{x}}^{c,1}$ as $\hat{\mathbf{z}}_A = [\hat{\mathbf{x}}^{p,i}, \hat{\mathbf{x}}^{c,1}, \hat{\boldsymbol{\Omega}}^{p,i}, \hat{\boldsymbol{\Omega}}^{c,1}]$, $C_A(\hat{\mathbf{z}} + \Delta\hat{\mathbf{z}}) = \|(\hat{\mathbf{x}}^i + \Delta\hat{\mathbf{x}}^i) - (\hat{\mathbf{x}}^{i+1} + \Delta\hat{\mathbf{x}}^{i+1})\|_2$ to enforce zero separation at the junction. To enable deformation propagation, a key observation is that many practical wire-harnesses feature junctions that are nearly rigid. This near-rigidity arises because manufacturers often use rigid plastics or other stiff materials at these connection points [33]. To capture this rigidity, we set $\hat{\mathbf{z}}_O = [\hat{\mathbf{x}}^{p,i}, \hat{\mathbf{x}}^{c,1}, \hat{\boldsymbol{\Omega}}^{p,i}, \hat{\boldsymbol{\Omega}}^{c,1}]$ and $C_O(\hat{\mathbf{z}}, \Delta\hat{\mathbf{z}}) = \|(\hat{\boldsymbol{\Omega}}^{p,i}(\hat{\mathbf{x}}, \Delta\hat{\mathbf{x}}) + \hat{\boldsymbol{\Omega}}_{\Delta}^{p,i}(\hat{\mathbf{x}}, \Delta\hat{\mathbf{x}})) - (\hat{\boldsymbol{\Omega}}^{c,1}(\hat{\mathbf{x}}, \Delta\hat{\mathbf{x}}) + \hat{\boldsymbol{\Omega}}_{\Delta}^{c,1}(\hat{\mathbf{x}}, \Delta\hat{\mathbf{x}}))\|_2 - \epsilon$, where $\hat{\boldsymbol{\Omega}}_{\Delta}$ and $\hat{\boldsymbol{\Omega}}$ are defined in Appendix B.2 and $\epsilon > 0$ bounds the mismatch between the updated parent-child orientation and the original orientation, ensuring that each junction remains *almost* rigid.

4.5 Algorithm Efficiency Improvement

Modeling speed is critical for efficient planning. However, as demonstrated in the experiments, directly implementing Algorithm 1 results in slow simulation and planning. This section presents two methods to significantly enhance computational performance.

Analytical Gradient Derivation: The goal of this subsection is to present the analytical gradient of $P(\Gamma(\mathbf{X}_t, \boldsymbol{\theta}_t), \alpha)$ with respect to $\boldsymbol{\theta}_t$. To improve the paper's readability, we summarize the result in the following theorem whose proof can be found in Appendix B.5.

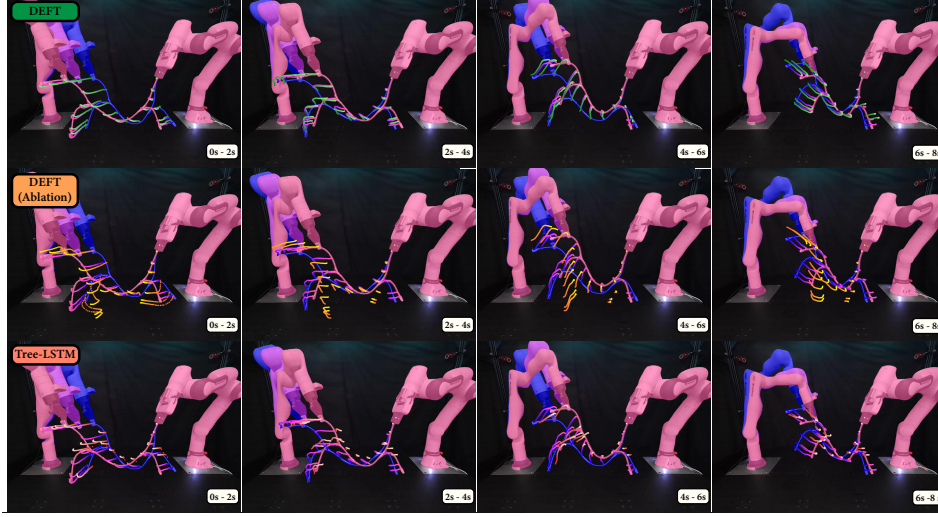


Figure 3: Visualization of predicted trajectories for BDLO 1 under scenarios where one robot grasps an end and the other grasps the midpoint, comparing DEFT, a DEFT ablation without enforcing junction near-rigidity (§4.4), and Tree-LSTM. Ground-truth vertex positions transition from blue (initial) to pink (final) via gradients indicating intermediate positions. Predictions similarly use gradients from dark to light. Ground truth is provided only at $t = 0$ s, with recursive predictions performed until $t = 8$ s without additional perception inputs.

Theorem 2. Let $\Gamma(\mathbf{X}_t, \boldsymbol{\theta}_t)$ be the Material Frame at time t , and let $\boldsymbol{\alpha}$ contain the bending stiffness $\mathbf{B} \in \mathbb{R}^{3 \times 3}$ and twisting stiffness $\beta \in \mathbb{R}$. Suppose the total potential energy is the sum of bending and twisting potential energies. The partial derivative of the bending and twisting potential energies with respect to θ^i are given by

$$\frac{\partial P_{\text{bend}}(\Gamma(\mathbf{X}_t, \boldsymbol{\theta}_t), \boldsymbol{\alpha})}{\partial \theta^i} = \sum_{k=i}^{i+1} (\mathbf{B}^k (\boldsymbol{\omega}^{(k,i)} - \bar{\boldsymbol{\omega}}^{(k,i)}))^T \cdot \begin{bmatrix} 0 & 1 \\ -1 & 0 \end{bmatrix} \boldsymbol{\omega}^{(k,i)}, \quad (8)$$

$$\frac{\partial P_{\text{twist}}(\Gamma(\mathbf{X}_t, \boldsymbol{\theta}_t), \boldsymbol{\alpha})}{\partial \theta^i} = \beta^i (\theta^i - \theta^{i-1}) - \beta^{i+1} (\theta^{i+1} - \theta^i), \quad (9)$$

respectively, where $\boldsymbol{\omega}^{(i,j)}$ is the material curvature.

Parallel Programming. Unlike quasi-static approaches [24, 25] that constantly require handling interactions between parent and child branches at each time step, DEFT constructs a computational graph that computes dynamics at junctions through constraints as post-processing. This strategy enables efficient parallel execution of Algorithm 1 (Lines 1-5 and 7) via PyTorch’s batch-wise operations, seamlessly integrating the physics-based framework with residual learning methods. To address dimensional mismatches between parent (n^p) and child (n^c) branches, we pad child branch matrices and vertices with zeros, ensuring uniform batch dimensions. Additionally, gradients from padded elements are masked during parameter updates to avoid influencing learned parameters.

5 Experiments and Results

Dataset Collection and Training. We collect dynamic trajectories for selected BDLOs using a motion capture system operating at 100 Hz, capturing both slow and fast motions. Data collection was divided into two categories: **Dataset 1:** Both robots grasped BDLO ends (for all BDLOs). **Dataset 2:** One robot grasped an end, and the other grasped the midpoint (for BDLOs 1 and 3). Experimental setup and data collection details are provided in Appendix C.1. Each method’s performance is evaluated when predicting the state of the wire over a 500 step (i.e. 5s) prediction horizon using just the state of the wire at $t = 0$ s and the orientation and position of the end effectors at each time step.

Baseline Comparisons. Only a limited number of studies have explored the dynamic behavior of BDLOs, and none provide publicly available code, making direct replication infeasible. We se-

Table 1: **Left:** Modeling Results Over a 5s Horizon. **Right:** Average Computational Time per 0.01 s Inference.

Method	Modeling Accuracy (RMSE, 10^{-2} m)						Computational Time (10^{-2} s)
	Dataset 1				Dataset 2		
	1	2	3	4	1	3	
GCN [8]	6.70	6.42	5.25	4.20	7.33	4.24	0.163
Tree-LSTM [31]	5.32	4.50	2.46	2.71	7.08	4.55	1.98
FEM [32]: Δ_t : 10^{-6} s, node: 60	3.11	3.70	2.29	2.84	2.17	2.10	493
FEM [32]: Δ_t : 10^{-6} s, node: 160	2.07	3.35	1.82	1.54	1.40	1.94	1211
FEM [32]: Δ_t : 10^{-2} s, node: 60	14.6	18.3	12.1	17.6	14.9	12.3	0.485
FEM [32]: Δ_t : 10^{-2} s, node: 160	12.9	15.1	10.0	11.8	12.8	9.71	1.09
DEFORM ⁺ [14]	4.59	7.44	5.02	4.46	3.88	4.25	1.665
DEFT	1.87	2.82	1.51	1.41	1.49	1.80	0.825

lect four implementations for comparison. **Learning-Based Modeling:** As BDLOs naturally map onto graph structures, architectures like Tree-LSTM [31] and GCN [8] could model their dynamics. **FEM-Based Modeling:** We selected FEM [32] as a baseline and optimized its parameters via grid search. Simulations varied timestep sizes from 1×10^{-2} s (DEFT’s setting) to 1×10^{-6} s and used 60 or 160 nodes, compared to DEFT’s ~ 20 . **DEFORM⁺:** To highlight DEFT’s contributions, we created DEFORM⁺, which extends DEFORM [14] to BDLOs by replacing DEFT’s junction constraints (§4.4) with FEM-based springs and bending. DEFORM⁺ excludes DEFT’s residual learning architecture (§4.3) and DEFT’s computational optimizations (§4.5). This is the most straightforward extension of DEFORM to BDLOs.

Modeling Results Table 1 (left) summarizes the average RMSE comparing DEFT to baselines across two dataset categories over a 5-second prediction horizon. DEFT outperforms all baselines in all but one case, where it is outperformed by the finest FEM. Figure 3 visualizes performance comparisons among DEFT, Tree-LSTM, and a DEFT ablation described later. Experimental videos are available in the supplementary material. Table 1 (right) summarizes average computational time for 0.01s inference. Table 1 indicates that GCN has the fastest speed. DEFT is the third fastest and is able to generate single step predictions above 100Hz frequency. In the planning task described later, DEFT completes each optimization loop **8.8** times faster than DEFORM++ and **1952** times faster than the finest FEM baseline. More experiments of computational speed are in Appendix C.3.

Ablation Study Table 2 highlights the impact of each DEFT contribution. Excluding all constraints introduced in §4.4 results in simulation instability. This outcome is primarily driven by the absence of inextensibility enforcement, which leads to simulation instability. Similarly, removing attachment constraints allows the children branch to detach from parent branch and fall freely, leading to a substantial increase in loss. Excluding near-rigidity constraints similarly reduces accuracy, underscoring the necessity of junction rigidity for effective dynamic propagation across branches. Note Although residual learning is used to mitigate errors, directly modeling stiff behaviors as described in §4.4, remains challenging, making the learning process highly sensitive to inputs and hampering effective gradient propagation. Neural networks alone struggle to maintain the system within the low-dimensional manifold defined by these constraints and minor errors can accumulate during open-loop predictions, reducing residual learning effectiveness. Despite these challenges, combination of auto-tuning the material properties and residual learning also provides the substantial improvement, illustrating DEFT’s ability to leverage real-world data for parameter identification and residual learning. By contrast, the model that do not learn from real-world data underperforms those that do, illustrating the importance of differentiability in this framework.

Shape Matching. In these experiments, we use BDLO 1 and employ ARMOUR [33], a receding-horizon trajectory planner and tracking controller, to manipulate the BDLO based on each model’s predictions. Integration details of ARMOUR with DEFT are in Appendix D. Each trial specifies a goal configuration and a random initial condition. A trial succeeds if each vertex reaches within 0.05 m of its target within 30 seconds. As shown in Table 3 (left), DEFT outperforms both baselines.

Table 2: Ablation Study with Dataset 1

Method	Modeling Accuracy (RSME, 10^{-2} m) \downarrow			
	Dataset 1			
	1	2	3	4
W/O Inext, Attach & Near-Rigidity	7.66×10^8	6.10×10^8	6.56×10^6	1.77×10^8
W/O Attach & Near-Rigidity	1.36×10^2	1.81×10^2	1.51×10^2	7.64×10^1
W/O Near-Rigidity	3.95	3.49	2.03	2.15
W/O Learning + System ID	2.46	3.53	1.85	1.77
W/O System ID	2.24	3.00	1.67	1.50
W/O Residual Learning	1.93	3.19	1.70	1.62
Full Model	1.87	2.82	1.51	1.41

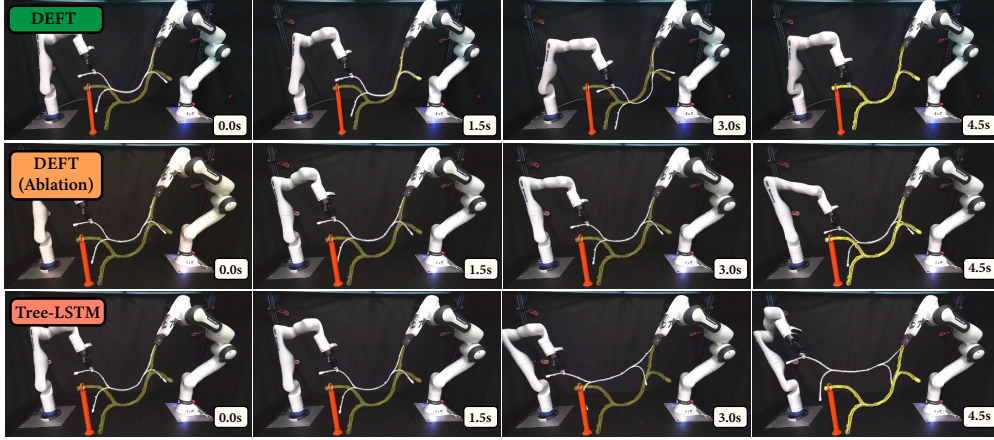


Figure 4: Visualization of planning for BDLO 1 for thread insertion, using DEFT, DEFT ablation without enforcing junction near-rigidity (§4.4), and Tree-LSTM. The BDLO’s goal configuration is highlighted in yellow, while the target hole is shown in red. The DEFT model enables the planning algorithm to successfully complete the task, whereas the ablation approach of DEFT and the Tree-LSTM model both fail to finish tasks.

Thread Insertion. In this experiment, the planning algorithm must insert the end of the BDLO into a hole of radius 2.5 cm which is placed in arbitrary location. The process consists of shape matching and thread insertion. Note that shape matching prevents deviations from the desired wire shape, avoiding excessive twisting or bending that could compromise safety and subsequent tasks (e.g., wire layout). Unlike the previous experiment, in which the robot grasps the branch end, the robot’s end effector clamps the third vertex from the branch’s insertion point. The trial is deemed successful if the BDLO branch passes through the torus while matching the user-specified wire shape. The results are summarized in Table 3 (right), and Figure 4 shows one of the real-world results.

Table 3: Real-World Trajectory Planning Results

Methods	Success Rate	
	Shape Matching	Insertion
Tree-LSTM [31]	2/40	0/35
DEFORM+ [14]	10/40	4/40
DEFT (Ablation)	27/40	16/35
DEFT	35/40	29/35

6 Conclusion

This paper introduces DEFT, a method embedding residual learning within a novel differentiable branched Deformable Linear Object (BDLO) simulator. DEFT delivers accurate modeling and real-time prediction of BDLO dynamic behavior during manipulation over extended time horizons. Compared to state-of-the-art approaches, DEFT achieves superior accuracy while maintaining sample efficiency and computational speed. We demonstrate DEFT’s integration with planning and control frameworks for 3D shape matching and thread insertion in real-world scenarios, successfully completing more complex manipulation tasks than other baselines.

7 Limitations

While DEFT demonstrates strong performance in modeling and controlling BDLOs, several areas for improvement remain. First, DEFT assumes the locations and geometries of the target insertion holes are known. This assumption may not hold in unstructured or partially observable environments. Incorporating advanced 3D scene understanding techniques, such as Gaussian Splatting [34], could improve system autonomy and adaptability. Second, DEFT occasionally fails at insertion tasks due to neglecting the gripper orientation during BDLO manipulation. As highlighted in [35], gripper orientation can affect a deformable object’s kinematics. Extending DEFT to explicitly model gripper orientation could enhance reliability. Lastly, DEFT does not explicitly handle interactions between deformable objects and their environment, such as contact forces and friction. Integrating contact modeling frameworks ([36]) would enable more accurate simulations and robust performance in scenarios involving frequent collisions or tight placements. Due to space constraints and the focused scope of this work, comprehensively addressing these limitations is deferred to future research.

8 Acknowledgement

The authors would like to gratefully thank the support by Ford Motor Company.

References

- [1] J. Sanchez, J.-A. Corrales, B.-C. Bouzgarrou, and Y. Mezouar. Robotic manipulation and sensing of deformable objects in domestic and industrial applications: a survey. *The International Journal of Robotics Research*, 37(7):688–716, 2018. doi:10.1177/0278364918779698. URL <https://doi.org/10.1177/0278364918779698>.
- [2] H. Wang, O. Salunkhe, W. Quadri, D. Lämkuhl, F. Ore, B. Johansson, and J. Stahre. Overview of computer vision techniques in robotized wire harness assembly: Current state and future opportunities. *Procedia CIRP*, 120:1071–1076, 2023. ISSN 2212-8271. doi:<https://doi.org/10.1016/j.procir.2023.09.127>. URL <https://www.sciencedirect.com/science/article/pii/S2212827123008594>. 56th CIRP International Conference on Manufacturing Systems 2023.
- [3] M. Saha and P. Isto. Manipulation planning for deformable linear objects. *IEEE Transactions on Robotics*, 23(6):1141–1150, 2007.
- [4] Z. et al. Challenges and outlook in robotic manipulation of deformable objects. *IEEE Robotics & Automation Magazine*, 2022.
- [5] M. Yan, Y. Zhu, N. Jin, and J. Bohg. Self-supervised learning of state estimation for manipulating deformable linear objects, 2020.
- [6] C. Wang, Y. Zhang, X. Zhang, Z. Wu, X. Zhu, S. Jin, T. Tang, and M. Tomizuka. Offline-online learning of deformation model for cable manipulation with graph neural networks. *IEEE Robotics and Automation Letters*, 7(2):5544–5551, Apr. 2022. ISSN 2377-3774. doi:10.1109/lra.2022.3158376. URL <http://dx.doi.org/10.1109/LRA.2022.3158376>.
- [7] K. Zhang, B. Li, K. Hauser, and Y. Li. Adaptigraph: Material-adaptive graph-based neural dynamics for robotic manipulation, 2024. URL <https://arxiv.org/abs/2407.07889>.
- [8] T. N. Kipf and M. Welling. Semi-supervised classification with graph convolutional networks, 2017.
- [9] T. Tang, Y. Fan, H.-C. Lin, and M. Tomizuka. Physics-informed neural networks: A deep learning framework for solving forward and inverse problems involving nonlinear partial differential equations. *Journal of Computational Physics*, 378:2427–2433, 2017. doi:10.1090/IROS.2017.8206058.
- [10] T. Bikmukhametov and J. Jäschke. Combining machine learning and process engineering physics towards enhanced accuracy and explainability of data-driven models. *Computers Chemical Engineering*, 138:106834, 2020. ISSN 0098-1354. doi:<https://doi.org/10.1016/j.compchemeng.2020.106834>. URL <https://www.sciencedirect.com/science/article/pii/S0098135419313675>.
- [11] A. Zeng, S. Song, J. Lee, A. Rodriguez, and T. Funkhouser. Tossingbot: Learning to throw arbitrary objects with residual physics. 2019.

- [12] B. Bianchini, M. Halm, and M. Posa. Simultaneous learning of contact and continuous dynamics. In *7th Annual Conference on Robot Learning*, 2023. URL https://openreview.net/forum?id=-3G6_D66Aua.
- [13] J. Gao, M. Y. Michelis, A. Spielberg, and R. K. Katzschmann. Sim-to-real of soft robots with learned residual physics, 2024.
- [14] Y. Chen, Y. Zhang, Z. Brei, T. Zhang, Y. Chen, J. Wu, and R. Vasudevan. Differentiable discrete elastic rods for real-time modeling of deformable linear objects. *arXiv preprint arXiv:2406.05931*, 2024.
- [15] Y. Wi, J. Lee, M. Oller, and N. Fazeli. Neural inverse source problems, 2024. URL <https://arxiv.org/abs/2411.01665>.
- [16] A. Theetten and L. Grisoni. A robust and efficient lagrangian constraint toolkit for the simulation of 1d structures. *Computer-Aided Design*, 41(12):990–998, 2009. ISSN 0010-4485. doi:<https://doi.org/10.1016/j.cad.2009.06.014>. URL <https://www.sciencedirect.com/science/article/pii/S001044850900195X>.
- [17] B. Nadler and M. B. Rubin. Post-buckling behavior of nonlinear elastic beams and three-dimensional frames using the theory of a cosserat point. *Mathematics and Mechanics of Solids*, 9(4):369–398, 2004. doi:[10.1177/1081286504033010](https://doi.org/10.1177/1081286504033010). URL <https://doi.org/10.1177/1081286504033010>.
- [18] Y. Zhao and J. Barbič. Interactive authoring of simulation-ready plants. *ACM Trans. Graph.*, 32(4), July 2013. ISSN 0730-0301. doi:[10.1145/2461912.2461961](https://doi.org/10.1145/2461912.2461961). URL <https://doi.org/10.1145/2461912.2461961>.
- [19] A. Nealen, M. Müller, R. Keiser, E. Boxerman, and M. Carlson. Physically based deformable models in computer graphics. *Comput. Graph. Forum*, 25:809–836, 12 2006. doi:[10.1111/j.1467-8659.2006.01000.x](https://doi.org/10.1111/j.1467-8659.2006.01000.x).
- [20] D. Baraff and A. Witkin. Large steps in cloth simulation. In *Proceedings of the 25th Annual Conference on Computer Graphics and Interactive Techniques*, SIGGRAPH ’98, page 43–54, New York, NY, USA, 1998. Association for Computing Machinery. ISBN 0897919998. doi:[10.1145/280814.280821](https://doi.org/10.1145/280814.280821). URL <https://doi.org/10.1145/280814.280821>.
- [21] F. S. Sin, D. Schroeder, and J. Barbič. Vega: non-linear fem deformable object simulator. In *Computer Graphics Forum*, volume 32, pages 36–48. Wiley Online Library, 2013.
- [22] A. Koessler, N. R. Filella, B.-C. Bouzgarrou, L. Lequière, and J.-A. C. Ramon. An efficient approach to closed-loop shape control of deformable objects using finite element models. In *2021 IEEE International Conference on Robotics and Automation (ICRA)*, pages 1637–1643. IEEE, 2021.
- [23] M. Bergou, M. Wardetzky, S. Robinson, B. Audoly, and E. Grinspun. Discrete elastic rods. In *ACM SIGGRAPH 2008 Papers*, SIGGRAPH ’08, New York, NY, USA, 2008. Association for Computing Machinery. ISBN 9781450301121. doi:[10.1145/1399504.1360662](https://doi.org/10.1145/1399504.1360662). URL <https://doi.org/10.1145/1399504.1360662>.
- [24] N. Umetani, R. Schmidt, and J. Stam. Position-based elastic rods. In *Proceedings of the ACM SIGGRAPH/Eurographics Symposium on Computer Animation*, SCA ’14, page 21–30, Goslar, DEU, 2015. Eurographics Association.
- [25] N. Lv, J. Liu, X. Ding, and H. Lin. Assembly simulation of multi-branch cables. *Journal of Manufacturing Systems*, 45:201–211, 2017. ISSN 0278-6125. doi:<https://doi.org/10.1016/j.jmsy.2017.09.007>. URL <https://www.sciencedirect.com/science/article/pii/S0278612517301346>.
- [26] H. Chen, J. Yang, D. Iascone, L. Liu, L. He, H. Peng, and J. Yao. Treemoco: Contrastive neuron morphology representation learning. In S. Koyejo, S. Mohamed, A. Agarwal, D. Belgrave, K. Cho, and A. Oh, editors, *Advances in Neural Information Processing Systems*, volume 35, pages 25060–25073. Curran Associates, Inc., 2022. URL https://proceedings.neurips.cc/paper_files/paper/2022/file/9f989633ffbd47a83caddac0f0261f-Paper-Conference.pdf.
- [27] L. Pineda, T. Fan, M. Monge, S. Venkataraman, P. Sodhi, R. T. Q. Chen, J. Ortiz, D. DeTone, A. Wang, S. Anderson, J. Dong, B. Amos, and M. Mukadam. Theseus: A library for differentiable nonlinear optimization, 2023.
- [28] A. Paszke, S. Gross, F. Massa, A. Lerer, J. Bradbury, G. Chanan, T. Killeen, Z. Lin, N. Gimeshein, L. Antiga, A. Desmaison, A. Köpf, E. Yang, Z. DeVito, M. Raison, A. Tejani, S. Chilamkurthy, B. Steiner, L. Fang, J. Bai, and S. Chintala. Pytorch: An imperative style, high-performance deep learning library, 2019.

- [29] J. Zhou, G. Cui, S. Hu, Z. Zhang, C. Yang, Z. Liu, L. Wang, C. Li, and M. Sun. Graph neural networks: A review of methods and applications, 2021. URL <https://arxiv.org/abs/1812.08434>.
- [30] M. Müller, B. Heidelberger, M. Hennix, and J. Ratcliff. Position based dynamics. *J. Vis. Commun. Image Represent.*, 18(2):109–118, apr 2007. ISSN 1047-3203. doi:10.1016/j.jvcir.2007.01.005. URL <https://doi.org/10.1016/j.jvcir.2007.01.005>.
- [31] K. S. Tai, R. Socher, and C. D. Manning. Improved semantic representations from tree-structured long short-term memory networks, 2015. URL <https://arxiv.org/abs/1503.00075>.
- [32] A. Nealen, M. Müller, R. Keiser, E. Boxerman, and M. Carlson. Physically based deformable models in computer graphics. *Computer Graphics Forum*, 25, 2006. URL <https://api.semanticscholar.org/CorpusID:15244087>.
- [33] J. Michaux, P. Holmes, B. Zhang, C. Chen, B. Wang, S. Sahgal, T. Zhang, S. Dey, S. Kousik, and R. Vasudevan. Can’t touch this: Real-time, safe motion planning and control for manipulators under uncertainty. *arXiv preprint arXiv:2301.13308*, 2023.
- [34] J. Michaux, S. Isaacson, C. E. Adu, A. Li, R. K. Swayampakula, P. Ewen, S. Rice, K. A. Skinner, and R. Vasudevan. Let’s make a splat: Risk-aware trajectory optimization in a normalized gaussian splat. *arXiv preprint arXiv:2409.16915*, 2024.
- [35] D. Berenson. Manipulation of deformable objects without modeling and simulating deformation. In *2013 IEEE/RSJ International Conference on Intelligent Robots and Systems*, pages 4525–4532, 2013. doi:10.1109/IROS.2013.6697007.
- [36] A. Choi, D. Tong, M. K. Jawed, and J. Joo. Implicit Contact Model for Discrete Elastic Rods in Knot Tying. *Journal of Applied Mechanics*, 88(5):051010, 03 2021. ISSN 0021-8936. doi:10.1115/1.4050238. URL <https://doi.org/10.1115/1.4050238>.
- [37] R. Bishop. There is more than one way to frame a curve. *The American Mathematical Monthly*, 82: Mathematical Association of America–, 03 1975. doi:10.2307/2319846.
- [38] W. H. Delashmit, L. M. Missiles, and M. T. Manry. Recent developments in multilayer perceptron neural networks. 2005. URL <https://api.semanticscholar.org/CorpusID:14200794>.
- [39] J. Trommnau, J. Kühnle, J. Siegert, R. Inderka, and T. Bauernhansl. Overview of the state of the art in the production process of automotive wire harnesses, current research and future trends. *Procedia CIRP*, 81:387–392, 2019. ISSN 2212-8271. doi:https://doi.org/10.1016/j.procir.2019.03.067. URL <https://www.sciencedirect.com/science/article/pii/S2212827119303725>. 52nd CIRP Conference on Manufacturing Systems (CMS), Ljubljana, Slovenia, June 12-14, 2019.

A Supplementary Material for DER Background

To model bending, twisting, and stretching, DER theory models DLOs using two key families of coordinate frames. First, it introduces Bishop Frames, which provide a twist-free reference state along the centerline of the rod. The Bishop Frame only rotates to follow the curve's geometry, providing a relaxed baseline configuration for the DLO. Second, the theory employs Material Frames, which describe the actual physical deformation of the rod. Material Frames can be expressed relative to the Bishop Frames through a single angle whose rate of change represents the physical twist of the DLO. To describe the twist of the DLO, DER theory assumes that the angle of the Material Frame with respect to the Bishop Frame is one that minimizes the potential energy of the DLO. We briefly summarize DER theory in this section, but a longer introduction can be found here [37].

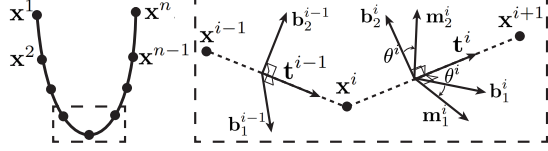


Figure 5: An illustration of DER coordinate frames.

Bishop Frame: The Bishop Frame at edge i is made up of three axes $\{t^i, b_1^i, b_2^i\}$. We next formally define each axis of the Bishop Frame. First, $t^i \in \mathbb{R}^3$ is the unit tangent along edge i which is defined as $t^i = (x^{i+1} - x^i) / \|x^{i+1} - x^i\|_2$. The vector $b_1^i \in \mathbb{R}^3$ is defined iteratively by applying a rotation matrix to the previous Bishop frame: $b_1^i = R^i \cdot b_1^{i-1}$. The rotation matrix $R^i \in \mathbb{R}^{3 \times 3}$ satisfies the following conditions

$$t^i = R^i \cdot t^{i-1} \quad (10)$$

$$t^{i-1} \times t^i = R^i \cdot (t^{i-1} \times t^i). \quad (11)$$

The first condition ensures that the tangent vector of the DLO at each subsequent edge can be described using the rotation matrix and the tangent vector at the previous edge. Though we do not prove it here, the second condition ensures that the rotation between successive Bishop Frames is minimal while moving along the DLO. In particular, this latter condition ensures that there is no twist about the subsequent tangent vectors at each edge of the DLO. Finally, $b_2^i := t^i \times b_1^i$, which ensures that b_2^i is orthogonal to t^i and b_1^i .

Material Frame: Subsequently, DER theory introduces Material Frames that are made up of three axes $\{t^i, m_1^i, m_2^i\}$. These Material Frames are generated by rotating the Bishop frame about the tangent vector by a scalar θ^i , i.e., m_1^i, m_2^i are defined as

$$m_1^i = b_1^i \cos \theta^i + b_2^i \sin \theta^i \quad (12)$$

$$m_2^i = -b_1^i \sin \theta^i + b_2^i \cos \theta^i \quad (13)$$

An illustration of the frames can be found in Figure 5.

Equations of Motion: DER theory assumes that the DLO reaches an equilibrium state between each simulation time step to obtain the optimal θ_t^* :

$$\theta_t^*(X_t, \alpha) = \arg \min_{\theta_t} P(\Gamma(X_t, \theta_t), \alpha) \quad (14)$$

Once $\theta_t^*(X_t, \alpha)$ is derived, the restorative force during deformation is given by the negative gradient of the potential energy with respect to the vertices. Consequently, the equation of motion for the DLO is:

$$M\ddot{X}_t = - \frac{\partial P(\Gamma(X_t, \theta_t^*(X_t, \alpha)), \alpha)}{\partial X_t} \quad (15)$$

One can numerically integrate this formula to predict the velocity and position by applying the Semi-Implicit Euler method:

$$\hat{V}_{t+1} = \hat{V}_t - \Delta_t M^{-1} \frac{\partial P(\Gamma(X_t, \theta_t^*(X_t, \alpha)), \alpha)}{\partial X_t}, \quad (16)$$

$$\hat{X}_{t+1} = \hat{X}_t + \Delta_t \hat{V}_{t+1}, \quad (17)$$

where $\Delta_t > 0$ is a user specified time discretization.

B Supplementary Material for the DEFT Algorithm

B.1 DEFT Contribution Visualization

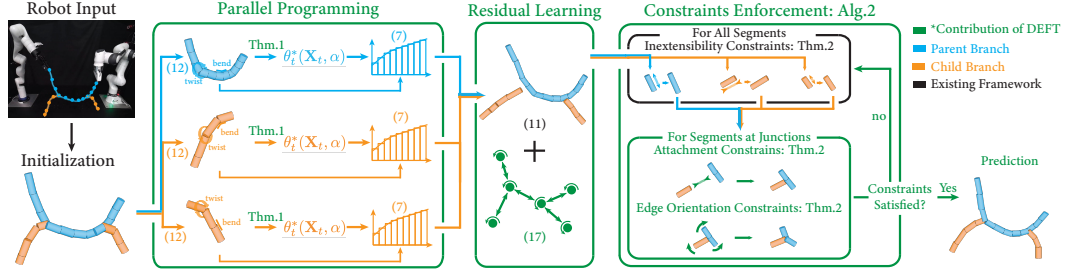


Figure 6: Overview of DEFT contributions. First, DEFT partitions the BDLO into parent and child DLOs, each discretized as elastic rods for accurate dynamic simulation (§4.1). It then predicts each branch’s dynamics in parallel (§4.5)—using analytical gradients to solve the inner loop for fast, stable convergence (§4.5). A GNN learns residual errors between simulated and observed behavior (§4.3), and constraint modules enforce inextensibility, junction attachments, and edge orientations for physical realism (§4.4). Inextensibility constraints are applied to each branch, while junction-level constraints ensure proper attachment at branch junctions. Additionally, edge orientation constraints enable the propagation of dynamics across these junctions. All components remain fully differentiable, enabling efficient parameter learning from real-world data.

B.2 Definition of $\hat{\Omega}_{\Delta,t}^i(\hat{\mathbf{X}}, \Delta\hat{\mathbf{X}})$ and $\hat{\Omega}^i$

In practice, it can be both challenging and impractical to attach hardware onto each segment for tracking its orientation changes. To address this limitation, we approximate the change in orientation, as illustrated in Figure 7. We define $\hat{\Omega}_{\Delta}^i(\hat{\mathbf{X}}, \Delta\hat{\mathbf{X}})$ as follows:

$$\hat{\Omega}_{\Delta}^i(\hat{\mathbf{X}}, \Delta\hat{\mathbf{X}}) = \frac{\hat{\mathbf{x}}^{i+1} - \hat{\mathbf{x}}^i}{\|\hat{\mathbf{x}}^{i+1} - \hat{\mathbf{x}}^i\|_2} \times \frac{(\hat{\mathbf{x}}^{i+1} + \Delta\hat{\mathbf{x}}^{i+1}) - (\hat{\mathbf{x}}^i + \Delta\hat{\mathbf{x}}^i)}{\|(\hat{\mathbf{x}}^{i+1} + \Delta\hat{\mathbf{x}}^{i+1}) - (\hat{\mathbf{x}}^i + \Delta\hat{\mathbf{x}}^i)\|_2} \quad (18)$$

Intuitively, the cross product of each edge’s tangent vector provides an approximation of the rotation axis and orientation change for the segment i . This approximation becomes more accurate when Δ_t is small.

Next, we describe how to compute $\hat{\Omega}^i$. Note that it is defined recursively using the computation at the previous time step. As a result just within this appendix, we add a subscript t to the symbol. To compute $\hat{\Omega}_{t+1}^i$, we first convert both $\hat{\Omega}_t^i$ and the correction rotation $\hat{\Omega}_{\Delta}^i(\hat{\mathbf{X}}_t, \Delta\hat{\mathbf{X}}_t)$ from angle-axis to quaternions. We then update $\hat{\Omega}_t^i$ by applying $\hat{\Omega}_{\Delta}^i(\hat{\mathbf{X}}_t, \Delta\hat{\mathbf{X}}_t)$ in quaternion form, and finally convert the result back to angle-axis coordinates to obtain $\hat{\Omega}_{t+1}^i$. Note that we do not continuously use quaternions because angle-axis is more convenient for representing angular momentum.

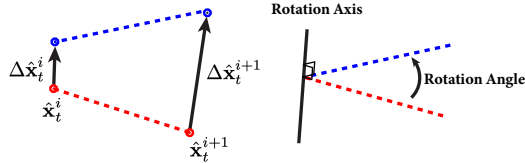


Figure 7: An illustration of $\hat{\Omega}_{\Delta}^i(\hat{\mathbf{X}}, \Delta\hat{\mathbf{X}})$

B.3 Residual Learning Details

The node feature matrix $\mathbf{F}_t(\hat{\mathbf{X}}_t, \hat{\mathbf{V}}_t, \alpha)$ is constructed by concatenating its arguments together. The trainable weight matrix $\mathbf{W} \in \mathbb{R}^{h \times 3}$ is implemented using a multi-layer perceptron (MLP) [38], consisting of two linear layers with a ReLU activation in between and a feature dimension of 64 for message passing. This projects input features into latent representations.

B.4 Supplementary Material for Enforcing Constraints

In what follows, we define $C(\hat{\mathbf{z}})$ for each constraint in Theorem 1, present the solutions as individual theorems with proofs, and summarize their enforcement in Algorithm 2.

B.4.1 Inextensibility Enforcement

To enforce inextensibility of each branch, we define a constraint function between successive vertices. This function penalizes deviations of each segment's length from its undeformed length. By applying the following theorem, one can compute $\Delta\hat{\mathbf{x}}^i, \Delta\hat{\mathbf{x}}^{i+1}$ explicitly:

Theorem 3 (Computing the Corrections to Enforce Inextensibility). *Consider two successive vertices i and $i + 1$ along the same branch. Let $\bar{\mathbf{e}}_i$ denote the edge between these vertices when the BDLO is undeformed. Let the constraint function to enforce inextensibility be defined as:*

$$C_I^i(\hat{\mathbf{X}}, \Delta\hat{\mathbf{X}}) = \|(\hat{\mathbf{x}}^i + \Delta\hat{\mathbf{x}}^i) - (\hat{\mathbf{x}}^{i+1} + \Delta\hat{\mathbf{x}}^{i+1})\|_2 - \|\bar{\mathbf{e}}_i\|_2. \quad (19)$$

The correction $\Delta\hat{\mathbf{X}}$ to enforce inextensibility at joint i can be computed by solving the following optimization problem:

$$\begin{aligned} \min_{\Delta\hat{\mathbf{X}}} \quad & \frac{1}{2} \left(C_I^i(\hat{\mathbf{X}}, \Delta\hat{\mathbf{X}}) \right)^2 \\ \text{s.t.} \quad & \Delta\hat{\mathbf{x}}^j = 0, \quad \forall j \notin \{i, i+1\}, \\ & \mathbf{M}^i \Delta\hat{\mathbf{x}}^i + \mathbf{M}^{i+1} \Delta\hat{\mathbf{x}}^{i+1} = \mathbf{0}, \\ & \mathbf{I}^i \hat{\Omega}_\Delta^i(\hat{\mathbf{X}}, \Delta\hat{\mathbf{X}}) = \mathbf{0}. \end{aligned} \quad (20)$$

where $\hat{\Omega}_\Delta^i(\hat{\mathbf{X}}, \Delta\hat{\mathbf{X}}) \in \mathbb{R}^3$ is defined in Appendix B.2 and represents the orientation change of the i th edge arising from $\Delta\hat{\mathbf{x}}^i$ and $\Delta\hat{\mathbf{x}}^{i+1}$ and $\mathbf{0}$ correspond to the zero vector of appropriate size. The only non-zero elements of the minimizer to this optimization problem can be computed explicitly and are equal to:

$$\Delta\hat{\mathbf{x}}^i = \mathbf{M}^{i+1} (\mathbf{M}^i + \mathbf{M}^{i+1})^{-1} C_I^i(\hat{\mathbf{X}}, \mathbf{0}) \frac{(\hat{\mathbf{x}}^{i+1} - \hat{\mathbf{x}}^i)}{\|\hat{\mathbf{x}}^{i+1} - \hat{\mathbf{x}}^i\|_2}, \quad (21)$$

$$\Delta\hat{\mathbf{x}}^{i+1} = \mathbf{M}^i (\mathbf{M}^i + \mathbf{M}^{i+1})^{-1} C_I^i(\hat{\mathbf{X}}, \mathbf{0}) \frac{(\hat{\mathbf{x}}^i - \hat{\mathbf{x}}^{i+1})}{\|\hat{\mathbf{x}}^{i+1} - \hat{\mathbf{x}}^i\|_2}. \quad (22)$$

Note that the inextensibility constraint at vertex i is satisfied when $C_I^i(\hat{\mathbf{X}}, \mathbf{0})^2 = 0$. For convenience, let the function that computes the minimizer of optimization problem (20) using $\hat{\mathbf{X}}$ be denoted by D_I^i (i.e., $D_I^i : \hat{\mathbf{X}} \mapsto \Delta\hat{\mathbf{X}}$).

Proof. The proof can be found in [14, Appendix B.2].

B.4.2 Enforcing Attachment at the Junction

To ensure the child branch remains attached to the parent branch, we define a constraint function between their junction vertices. By applying the following theorem, one can compute $\Delta\hat{\mathbf{x}}^{p,i}, \Delta\hat{\mathbf{x}}^{c,1}$ explicitly:

Theorem 4. *Consider the parent-branch vertex $\hat{\mathbf{x}}^{p,i}$ and child-branch vertex $\hat{\mathbf{x}}^{c,1}$ at the junction such as the one depicted in Figure 2. Let the constraint function to enforce attachment at the junction be defined as:*

$$C_A^{p,i}(\hat{\mathbf{X}}, \Delta\hat{\mathbf{X}}) = \|(\hat{\mathbf{x}}^{p,i} + \Delta\hat{\mathbf{x}}^{p,i}) - (\hat{\mathbf{x}}^{c,1} + \Delta\hat{\mathbf{x}}^{c,1})\|_2. \quad (23)$$

Suppose that the correction $\Delta\hat{\mathbf{X}}$ to account for the junction attachment constraint is obtained by solving an optimization problem that is identical to (20) with the objective function replaced with (23) and with a requirement that the only elements of $\Delta\hat{\mathbf{X}}$ are those associated vertices p, i and $c, 1$.

The only non-zero elements of the minimizer to this optimization problem can be computed explicitly and are equal to:

$$\Delta \hat{\mathbf{x}}^{p,i} = \mathbf{M}^{c,1} (\mathbf{M}^{p,i} + \mathbf{M}^{c,1})^{-1} C_A^{p,i}(\hat{\mathbf{X}}, \mathbf{0}) \frac{(\hat{\mathbf{x}}^{c,1} - \hat{\mathbf{x}}^{p,i})}{\|\hat{\mathbf{x}}^{c,1} - \hat{\mathbf{x}}^{p,i}\|_2}, \quad (24)$$

$$\Delta \hat{\mathbf{x}}^{c,1} = \mathbf{M}^{p,i} (\mathbf{M}^{p,i} + \mathbf{M}^{c,1})^{-1} C_A^{p,i}(\hat{\mathbf{X}}, \mathbf{0}) \frac{(\hat{\mathbf{x}}^{p,i} - \hat{\mathbf{x}}^{c,1})}{\|\hat{\mathbf{x}}^{c,1} - \hat{\mathbf{x}}^{p,i}\|_2}. \quad (25)$$

Note that the junction attachment constraint is satisfied at vertex p, i when $C_I^{p,i}(\hat{\mathbf{X}}, \mathbf{0})^2 = 0$. For convenience, let the function that computes the minimizer of optimization problem (20) using $\hat{\mathbf{X}}$ be denoted by $D_A^{p,i}$ (i.e., $D_A^{p,i} : \hat{\mathbf{X}} \mapsto \Delta \hat{\mathbf{X}}$).

Proof. To prove Theorem 4, we first formulate the optimization problem:

$$\min_{\Delta \hat{\mathbf{X}}} \frac{1}{2} \left(C_A^{p,i}(\hat{\mathbf{X}}, \Delta \hat{\mathbf{X}}) \right)^2 \quad (26)$$

$$\text{s.t. } \Delta \hat{\mathbf{x}}^j = \mathbf{0}, \quad \forall j \notin \{(p, i), (c, 1)\}, \quad (27)$$

$$\mathbf{M}^{p,i} \Delta \hat{\mathbf{x}}^{p,i} + \mathbf{M}^{c,1} \Delta \hat{\mathbf{x}}^{c,1} = \mathbf{0}, \quad (28)$$

$$\mathbf{I}^{p,i} \hat{\Omega}_\Delta^{p,i}(\hat{\mathbf{X}}, \Delta \hat{\mathbf{X}}) = \mathbf{0}. \quad (29)$$

To solve the above optimization, we introduce Lagrange multipliers $\lambda_l \in \mathbb{R}^3$ and $\lambda_r \in \mathbb{R}^3$ associated with constraints (28) and (29), respectively. The corresponding Lagrangian \mathcal{L} can be found as follow:

$$\begin{aligned} \mathcal{L}(\Delta \hat{\mathbf{x}}^{p,i}, \Delta \hat{\mathbf{x}}^{c,1}, \lambda_l, \lambda_r) = & \frac{1}{2} \left(C_A^{p,i}(\hat{\mathbf{X}}, \Delta \hat{\mathbf{X}}) \right)^2 - \\ & \lambda_l^T (\mathbf{M}^i \Delta \hat{\mathbf{x}}^{p,i} + \mathbf{M}^{c,1} \Delta \hat{\mathbf{x}}^{c,1}) - \lambda_r^T \mathbf{I}^{p,i} \hat{\Omega}_\Delta^{p,i}(\hat{\mathbf{X}}, \Delta \hat{\mathbf{X}}) \end{aligned} \quad (30)$$

Next, we take the partial derivatives of (30) with respect to $\Delta \hat{\mathbf{x}}^{p,i}$, $\Delta \hat{\mathbf{x}}^{c,1}$, λ_l , λ_r . Setting each derivative to zero yields the system of equations (31), (32), (33), and (34).

$$\begin{aligned} \frac{\partial \mathcal{L}(\Delta \hat{\mathbf{x}}^{p,i}, \Delta \hat{\mathbf{x}}^{c,1}, \lambda_l, \lambda_r)}{\partial \Delta \hat{\mathbf{x}}^{p,i}} = & C_A^{p,i}(\hat{\mathbf{X}}, \Delta \hat{\mathbf{X}}) \frac{(\hat{\mathbf{x}}^{p,i} + \Delta \hat{\mathbf{x}}^{p,i}) - (\hat{\mathbf{x}}^{c,1} + \Delta \hat{\mathbf{x}}^{c,1})}{\|(\hat{\mathbf{x}}^{p,i} + \Delta \hat{\mathbf{x}}^{p,i}) - (\hat{\mathbf{x}}^{c,1} + \Delta \hat{\mathbf{x}}^{c,1})\|_2} - \lambda_l^T \mathbf{M}^{p,i} - \frac{\partial \lambda_r^T \mathbf{I}^{p,i} \hat{\Omega}_\Delta^{p,i}(\hat{\mathbf{X}}, \Delta \hat{\mathbf{X}})}{\partial \Delta \hat{\mathbf{x}}^{p,i}} = \mathbf{0} \end{aligned} \quad (31)$$

$$\begin{aligned} \frac{\partial \mathcal{L}(\Delta \hat{\mathbf{x}}^{p,i}, \Delta \hat{\mathbf{x}}^{c,1}, \lambda_l, \lambda_r)}{\partial \Delta \hat{\mathbf{x}}^{c,1}} = & C_A^{p,i}(\hat{\mathbf{X}}, \Delta \hat{\mathbf{X}}) \frac{(\hat{\mathbf{x}}^{c,1} + \Delta \hat{\mathbf{x}}^{c,1}) - (\hat{\mathbf{x}}^{p,i} + \Delta \hat{\mathbf{x}}^{p,i})}{\|(\hat{\mathbf{x}}^{p,i} + \Delta \hat{\mathbf{x}}^{p,i}) - (\hat{\mathbf{x}}^{c,1} + \Delta \hat{\mathbf{x}}^{c,1})\|_2} - \lambda_l^T \mathbf{M}^{c,1} - \frac{\partial \lambda_r^T \mathbf{I}^{p,i} \hat{\Omega}_\Delta^{p,i}(\hat{\mathbf{X}}, \Delta \hat{\mathbf{X}})}{\partial \Delta \hat{\mathbf{x}}^{c,1}} = \mathbf{0} \end{aligned} \quad (32)$$

$$\frac{\partial \mathcal{L}(\Delta \hat{\mathbf{x}}^{p,i}, \Delta \hat{\mathbf{x}}^{c,1}, \lambda_l, \lambda_r)}{\partial \lambda_l} = -(\mathbf{M}^i \Delta \hat{\mathbf{x}}^{p,i} + \mathbf{M}^{c,1} \Delta \hat{\mathbf{x}}^{c,1}) = \mathbf{0} \quad (33)$$

$$\frac{\partial \mathcal{L}(\Delta \hat{\mathbf{x}}^{p,i}, \Delta \hat{\mathbf{x}}^{c,1}, \lambda_l, \lambda_r)}{\partial \lambda_r} = -\mathbf{I}^T \lambda_r^T \mathbf{I}^{p,i} \hat{\Omega}_\Delta^{p,i}(\hat{\mathbf{X}}, \Delta \hat{\mathbf{X}}) = \mathbf{0} \quad (34)$$

We first observe that solving (33) leads to the following equation:

$$\Delta \hat{\mathbf{x}}^{c,1} = -(\mathbf{M}^{c,1})^{-1} \mathbf{M}^{p,i} \Delta \hat{\mathbf{x}}^{p,i} \quad (35)$$

This indicates that $\Delta \hat{\mathbf{x}}^{p,i}$, $\Delta \hat{\mathbf{x}}^{c,1}$ are colinear. Based on the definition of $\hat{\Omega}_\Delta^i(\hat{\mathbf{X}}, \Delta \hat{\mathbf{X}})$ in Appendix B.2, one can see that if $\Delta \hat{\mathbf{x}}^{p,i}$, $\Delta \hat{\mathbf{x}}^{c,1}$ are colinear, then $\hat{\Omega}_\Delta^{p,i}(\hat{\mathbf{X}}, \Delta \hat{\mathbf{X}}) = \mathbf{0}$. Note that this is

true regardless of the size of Δ_t . Hence, it naturally satisfies (34). Next, summing (31) with (32) yields the following:

$$\lambda_l \mathbf{M}^{p,i} + \lambda_l \mathbf{M}^{c,1} = \mathbf{0} \quad (36)$$

As mass matrices are always positive definite. This indicates $\lambda_l = \mathbf{0}$. Based on (31), (35) and (36), solving for $\Delta \hat{\mathbf{x}}^{p,i}$ is equivalent to solving the following equation:

$$C_A^{p,i}(\hat{\mathbf{X}}, \Delta \hat{\mathbf{X}}) = \mathbf{0} \quad (37)$$

After applying some algebraic manipulations, $\Delta \hat{\mathbf{x}}^{p,i}$ can be found to be:

$$\Delta \hat{\mathbf{x}}^{p,i} = \mathbf{M}^{c,1} (\mathbf{M}^{p,i} + \mathbf{M}^{c,1})^{-1} C_A^{p,i}(\hat{\mathbf{X}}, \mathbf{0}) \frac{(\hat{\mathbf{x}}^{c,1} - \hat{\mathbf{x}}^{p,i})}{\|\hat{\mathbf{x}}^{c,1} - \hat{\mathbf{x}}^{p,i}\|_2},$$

Using $\Delta \hat{\mathbf{x}}^{p,i}$ and (35), one can find:

$$\Delta \hat{\mathbf{x}}^{c,1} = \mathbf{M}^{p,i} (\mathbf{M}^{p,i} + \mathbf{M}^{c,1})^{-1} C_A^{p,i}(\hat{\mathbf{X}}, \mathbf{0}) \frac{(\hat{\mathbf{x}}^{p,i} - \hat{\mathbf{x}}^{c,1})}{\|\hat{\mathbf{x}}^{c,1} - \hat{\mathbf{x}}^{p,i}\|_2}.$$

B.4.3 Edge Orientation Constraints

Many practical wire-harnesses feature junctions that are nearly rigid. This near-rigidity arises because manufacturers often use rigid plastics or other stiff materials at these connection points [39]. This results in minimal rotational or bending freedom. Consequently, the dynamics between the parent and child branches propagate through the junction in an almost rigid manner. To capture this behavior, we model each edge as a rigid body and define a constraint function that computes the relative orientation of each body. We then require that this constraint function is approximately satisfied. One can compute $\Delta \hat{\mathbf{x}}^{p,i}$, $\Delta \hat{\mathbf{x}}^{c,1}$ explicitly:

Theorem 5. Consider the parent-branch vertex $\hat{\mathbf{x}}^{p,i}$ and child-branch vertex $\hat{\mathbf{x}}^{c,1}$ at the junction such as the one depicted in Figure 2. Let $\epsilon > 0$ be a user specified parameter. Let the constraint function to enforce the orientation of the junction be defined as:

$$C_O^{p,i}(\hat{\mathbf{X}}, \Delta \hat{\mathbf{X}}) = \|(\hat{\Omega}^{p,i}(\hat{\mathbf{X}}, \Delta \hat{\mathbf{X}}) + \hat{\Omega}_\Delta^{p,i}(\hat{\mathbf{X}}, \Delta \hat{\mathbf{X}})) - (\hat{\Omega}^{c,i}(\hat{\mathbf{X}}, \Delta \hat{\mathbf{X}}) + \hat{\Omega}_\Delta^{c,i}(\hat{\mathbf{X}}, \Delta \hat{\mathbf{X}}))\|_2 - \epsilon, \quad (38)$$

where $\hat{\Omega}_\Delta$ and $\hat{\Omega}$ are defined in Appendix B.2 and $\epsilon > 0$ bounds the mismatch between the updated parent-child orientation and the original orientation, ensuring that each junction remains almost rigid. The orientation correction at the junction is obtained by solving the following optimization problem:

$$\min_{\Delta \hat{\mathbf{X}}} \frac{1}{2} \left(C_O^{p,i}(\hat{\mathbf{X}}, \Delta \hat{\mathbf{X}}) \right)^2 \quad (39)$$

$$\text{s.t. } \mathbf{I}^{p,i} \hat{\Omega}_\Delta^{p,i} + \mathbf{I}^{c,1} \hat{\Omega}_\Delta^{c,1} = \mathbf{0} \quad (40)$$

When Δ_t is sufficiently small, explicit formulas for $\Delta \hat{\mathbf{X}}$ can be computed as follows:

$$\hat{\Omega}_\Delta^{p,i} = \mathbf{I}^{c,1} (\mathbf{I}^{c,1} + \mathbf{I}^{p,i})^{-1} C_O^{p,i}(\hat{\mathbf{X}}, \mathbf{0}) \frac{\hat{\Omega}^{c,1} - \hat{\Omega}^{p,i}}{\|\hat{\Omega}^{c,1} - \hat{\Omega}^{p,i}\|_2}, \quad (41)$$

$$\hat{\Omega}_\Delta^{c,1} = \mathbf{I}^{p,i} (\mathbf{I}^{c,1} + \mathbf{I}^{p,i})^{-1} C_O^{p,i}(\hat{\mathbf{X}}, \mathbf{0}) \frac{\hat{\Omega}^{p,i} - \hat{\Omega}^{c,1}}{\|\hat{\Omega}^{c,1} - \hat{\Omega}^{p,i}\|_2}. \quad (42)$$

Once $\hat{\Omega}_\Delta^{p,i}$, $\hat{\Omega}_\Delta^{c,1}$ are obtained, an approach described in the following are used to update $\hat{\mathbf{x}}^{p,i}$ and $\hat{\mathbf{x}}^{c,1}$ accordingly. Note that the junction orientation constraint is satisfied at vertex p, i when $C_O^{p,i}(\hat{\mathbf{X}}, \mathbf{0})^2 = 0$. For convenience, let the function that computes the minimizer of optimization problem (20) using $\hat{\mathbf{X}}$ be denoted by $D_O^{p,i}$ (i.e., $D_O^{p,i} : \hat{\mathbf{X}} \mapsto \Delta \hat{\mathbf{X}}$).

Proof. For convenience in the proof, we suppress the arguments to functions for convenience. To prove Theorem 5, we begin by describing how $\hat{\Omega}_\Delta^i$ is applied to rotate the i -th segment. Note that Δ_t should be sufficiently small for $\hat{\Omega}_\Delta^i$ to accurately approximate the change in orientation. As shown

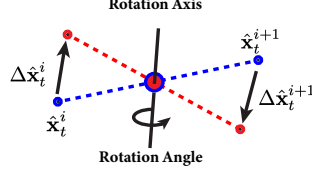


Figure 8: An illustration of applying $\hat{\Omega}_{\Delta}^i$ to rotate the i -th segment.

in Figure 8, the rotation axis coincides with the center of the i -th segment. In practice, the rotation of the i -th segment is achieved by converting $\hat{\Omega}_{\Delta}^i$ into the rotation matrix $\hat{\Omega}_{\Delta}^i \mapsto \mathbf{R}_{\Delta}^i$. Consequently, we obtain $\Delta \hat{\mathbf{x}}^i$ and $\Delta \hat{\mathbf{x}}^{i+1}$ via

$$\Delta \hat{\mathbf{x}}^i = \mathbf{R}_{\Delta}^i \frac{(\hat{\mathbf{x}}^{i+1} - \hat{\mathbf{x}}^i)}{2}, \quad (43)$$

$$\Delta \hat{\mathbf{x}}^{i+1} = \mathbf{R}_{\Delta}^i \frac{(\hat{\mathbf{x}}^i - \hat{\mathbf{x}}^{i+1})}{2}. \quad (44)$$

Because each segment rotates only about its own center, linear momentum is naturally conserved. Thus, we can simplify the optimization problem and write the following optimization problem:

$$\begin{aligned} \min_{\Delta \hat{\mathbf{X}}} \quad & \frac{1}{2} \left(C_O^{p,i}(\hat{\mathbf{X}}, \Delta \hat{\mathbf{X}}) \right)^2 \\ \text{s.t.} \quad & \mathbf{I}^{p,i} \hat{\Omega}_{\Delta}^{p,i} + \mathbf{I}^{c,1} \hat{\Omega}_{\Delta}^{c,1} = \mathbf{0} \end{aligned} \quad (45)$$

where (38), (39), and (40) are analogous to (23), (26), and (28), respectively. Next, we introduce a Lagrange multiplier and follow the same derivation steps as in (31), (35), and (36), which leads to:

$$\begin{aligned} \hat{\Omega}_{\Delta}^{p,i} &= \mathbf{I}^{c,1} (\mathbf{I}^{c,1} + \mathbf{I}^{p,i})^{-1} C_O^{p,i}(\hat{\mathbf{X}}, \mathbf{0}) \frac{\hat{\Omega}^{c,1} - \hat{\Omega}^{p,i}}{\|\hat{\Omega}^{c,1} - \hat{\Omega}^{p,i}\|_2}, \\ \hat{\Omega}_{\Delta}^{c,1} &= \mathbf{I}^{p,i} (\mathbf{I}^{c,1} + \mathbf{I}^{p,i})^{-1} C_O^{p,i}(\hat{\mathbf{X}}, \mathbf{0}) \frac{\hat{\Omega}^{p,i} - \hat{\Omega}^{c,1}}{\|\hat{\Omega}^{c,1} - \hat{\Omega}^{p,i}\|_2}. \end{aligned}$$

Once $\hat{\Omega}_{\Delta}^{p,i}, \hat{\Omega}_{\Delta}^{c,1}$ are obtained, (43) and (44) are used to update $\hat{\mathbf{x}}^{p,i}$ and $\hat{\mathbf{x}}^{c,1}$ accordingly.

B.4.4 Algorithm to Implement Corrections Due To Constraint Enforcement

As described earlier, we run each of these optimization problems sequentially to generate a correction to the output of the integration method (Line 5 in Algorithm 1). This is summarized in Algorithm 2. Note that one begins by checking whether any constraint is violated by more than some user-specified parameter κ . If any of the constraints are violated by more than κ , then one applies the correction described in the previous subsections to modify the prediction. This repeats until all constraints are satisfied.

B.5 Proof of Theorem 2

To prove the theorem, we begin by introducing the curvature binormal and material curvature.

Material Curvatures: The curvature binormal $\kappa \mathbf{b}^i$ is traditionally used to represent the turning angle and axis between two consecutive edges:

$$\kappa \mathbf{b}^i = \frac{2 \mathbf{e}^{i-1} \times \mathbf{e}^i}{\|\mathbf{e}^{i-1}\|_2 \|\mathbf{e}^i\|_2 + \mathbf{e}^{i-1} \cdot \mathbf{e}^i}, \quad (46)$$

where \mathbf{e}^{i-1} and \mathbf{e}^i are consecutive edge vectors, \times denotes the cross product, and \cdot denotes the dot product. By incorporating the material frame (12) and (13), the curvature binormal (46) is projected onto the material frame to quantify the extent to which the curvature aligns with the frame's orientation. This projection, which we call the material curvature, provides additional insights into

Algorithm 2 Momentum Preserving Constraint Enforcement

Require: $\hat{\mathbf{X}}_{t+1}, \kappa > 0$

```

1: while  $\exists(i, j)$  such that  $C_j^i(\hat{\mathbf{X}}_{t+1}, \mathbf{0})^2 > \kappa$  do
2:   for  $i = 1$  to  $n - 1$  do
3:      $\hat{\mathbf{X}}_{t+1} = \hat{\mathbf{X}}_{t+1} + D_I^i(\hat{\mathbf{X}}_{t+1})$  ▷ Theorem 3
4:     if  $i$ th segments is a junction then
5:        $\hat{\mathbf{X}}_{t+1} = \hat{\mathbf{X}}_{t+1} + D_A^i(\hat{\mathbf{X}}_{t+1})$  ▷ Theorem 4
6:        $\hat{\mathbf{X}}_{t+1} = \hat{\mathbf{X}}_{t+1} + D_O^i(\hat{\mathbf{X}}_{t+1})$  ▷ Theorem 5
7:     end if
8:   end for
9: end while
10: return :  $\hat{\mathbf{X}}_t$  ▷ Updated Vertices

```

the deformation characteristics, allowing us to distinguish between bending and twisting behaviors within the material frame and is defined as:

$$\omega^{(i,j)} = \left(\kappa \mathbf{b}^i \cdot \mathbf{m}_1^j, \kappa \mathbf{b}^i \cdot \mathbf{m}_2^j \right)^T \quad \text{for } j \in \{i-1, i\}. \quad (47)$$

Potential Energy: The potential energy is composed of the bending energy and twisting energy:

$$P(\Gamma(\mathbf{X}_t, \boldsymbol{\theta}_t), \boldsymbol{\alpha}) = P_{\text{bend}}(\Gamma(\mathbf{X}_t, \boldsymbol{\theta}_t), \boldsymbol{\alpha}) + P_{\text{twist}}(\Gamma(\mathbf{X}_t, \boldsymbol{\theta}_t), \boldsymbol{\alpha}), \quad (48)$$

where

$$P_{\text{bend}}(\Gamma(\mathbf{X}_t, \boldsymbol{\theta}_t), \boldsymbol{\alpha}) = \sum_{i=1}^{n-1} \sum_{j=i-1}^i \frac{1}{2} \left(\omega^{(i,j)} - \bar{\omega}^{(i,j)} \right)^T \mathbf{B}^j \left(\omega^{(i,j)} - \bar{\omega}^{(i,j)} \right), \quad (49)$$

and

$$P_{\text{twist}}(\Gamma(\mathbf{X}_t, \boldsymbol{\theta}_t), \boldsymbol{\alpha}) = \sum_{i=1}^{n-1} \frac{1}{2} \beta^i (\theta^i - \theta^{i-1})^2, \quad (50)$$

where $\bar{\omega}^{(i,j)}$ denotes the undeformed material curvature, which is calculated when the DLO is in a static state without any external or internal forces applied, and \mathbf{B} and β , are components of $\boldsymbol{\alpha}$, representing the bending stiffness and twisting stiffness, respectively.

Gradient of Potential Energy: With (49) and (50), the gradient of (48) can be derived as following:

$$\frac{\partial P(\Gamma(\mathbf{X}_t, \boldsymbol{\theta}_t), \boldsymbol{\alpha})}{\partial \theta^i} = \frac{\partial P_{\text{bend}}(\Gamma(\mathbf{X}_t, \boldsymbol{\theta}_t), \boldsymbol{\alpha})}{\partial \theta^i} + \frac{\partial P_{\text{twist}}(\Gamma(\mathbf{X}_t, \boldsymbol{\theta}_t), \boldsymbol{\alpha})}{\partial \theta^i} \quad (51)$$

We begin by deriving the first term. Note that θ^i is only relevant in $\omega^{(i,i)}$ and $\omega^{(i+1,i)}$. Using the chain rule, we obtain:

$$\frac{\partial P_{\text{bend}}(\Gamma(\mathbf{X}_t, \boldsymbol{\theta}_t), \boldsymbol{\alpha})}{\partial \theta^i} = \sum_{k=i}^{i+1} \frac{\partial P_{\text{bend}}(\Gamma(\mathbf{X}_t, \boldsymbol{\theta}_t), \boldsymbol{\alpha})}{\partial \omega^{(k,i)}} \frac{\partial \omega^{(k,i)}}{\partial \theta^i}. \quad (52)$$

To compute $\frac{\partial \omega^{(k,i)}}{\partial \theta^i}$, we use the identities $\frac{\partial \mathbf{m}_1^i}{\partial \theta^i} = \mathbf{m}_2^i$ and $\frac{\partial \mathbf{m}_2^i}{\partial \theta^i} = -\mathbf{m}_1^i$. These lead to:

$$\frac{\partial \omega^{(k,i)}}{\partial \theta^i} = \begin{bmatrix} 0 & 1 \\ -1 & 0 \end{bmatrix} \omega^{(k,i)} \quad (53)$$

Substituting this result back, we obtain:

$$\frac{\partial P_{\text{bend}}(\Gamma(\mathbf{X}_t, \boldsymbol{\theta}_t), \boldsymbol{\alpha})}{\partial \theta^i} = \sum_{k=i}^{i+1} (\mathbf{B}^k (\omega^{(k,i)} - \bar{\omega}^{(k,i)}))^T \cdot \begin{bmatrix} 0 & 1 \\ -1 & 0 \end{bmatrix} \omega^{(k,i)}, \quad (54)$$

The second term of (51) can be derived, resulting in:

$$\frac{\partial P_{\text{twist}}(\Gamma(\mathbf{X}_t, \boldsymbol{\theta}_t), \boldsymbol{\alpha})}{\partial \theta^i} = \beta^i (\theta^i - \theta^{i-1}) - \beta^{i+1} (\theta^{i+1} - \theta^i) \quad (55)$$

By substituting (54) and (55) into (51), we obtain the analytical gradient of the potential energy.

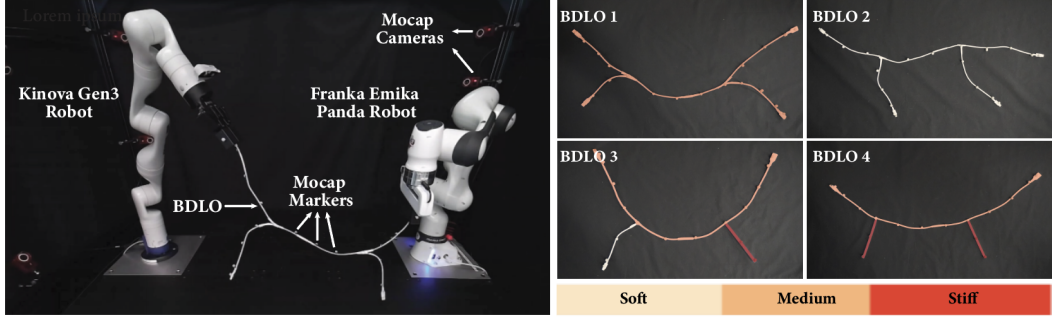


Figure 9: An illustration of experiment setup. **Left:** Data collection setup with a dual-arm robot. **Right:** An illustration of the BDLOs used to evaluate and compare the performance of DEFT against baseline methods. To increase dataset diversity, we vary the BDLOs’ stiffness, length, weights, number of vertices, and junction structures.

Table 4: A summary of each BDLO’s material properties and marker count used in the real-world experiment. Stiffness is estimated based on a relative scale.

BDLO	Parent Stiffness / #Markers	Child1 Stiffness / #Markers	Child2 Stiffness / #Markers	Dataset 1 Time (s)	Dataset 2 Time (s)
1	Medium / 13	Medium / 4	Medium / 3	505	440
2	Low / 12	Low / 4	Low / 4	735	N/A
3	Medium / 12	Low / 2	High / 3	645	445
4	Medium / 12	High / 2	High / 2	495	N/A

C Supplementary Material for Experiments

C.1 Hardware Setup

Four distinct BDLOs were constructed to validate DEFT’s modeling accuracy as shown at the bottom of Figure 9. The material stiffness description of each BDLO is outlined in Table 4. Note that we introduced stiff child branches attached to the parent branch in BDLO3 and BDLO4. These branches represent the rigid components (e.g., fixations) commonly used in BDLO construction [39]. These attachments help ensure secure mounting, preserve structural integrity, and manage loads in real-world applications. Note that we selected two child branches for each BDLO to evaluate DEFT’s performance across combinations of branches with varying stiffness. However, our methodology is theoretically scalable to BDLOs with arbitrary tree-like topologies. Spherical markers were attached to each BDLO to facilitate dataset creation for both training and evaluation, with the number of vertices set equal to the number of MoCap markers. Because the markers are present during both training and evaluation, their impact on the BDLO dynamics is inherently accounted within all subsequent analyses. If one wishes to obtain a BDLO dataset without relying on real-world motion capture, a finite element method-based simulator could be employed. Note that the markers are *only* used to create training and evaluation datasets, as well as evaluate the performance of DEFT by providing the ground truth. However, for real-world applications, the markers are not needed. For dual manipulation, a Franka Emika Research 3 robot and a Kinova Gen3 robot were used. An illustration of the experimental setup is shown in Figure 9. We used an OptiTrack motion capture system to record ground-truth vertex locations. Note in our implementation of DEFT we set $\epsilon = 0.1$ (Theorem 5) and $\kappa = 0.02$ (Algorithm 2). The parameters were selected to balance stability, convergence speed, and accuracy. The dataset is split with $\sim 75\%$ for training and $\sim 25\%$ for evaluation.

C.2 Training Setup

Let $\mathbf{U}_{1:T-1}$ denote the set of inputs applied from time $t = 1$ to $t = T - 1$, and let $\mathbf{X}_{1:T} = \{\mathbf{X}_1, \mathbf{X}_2, \dots, \mathbf{X}_T\} \in \mathbb{R}^{T \times n \times 3}$ denote the corresponding ground-truth trajectory of the BDLO from

$t = 1$ to $t = T$. Given known initial conditions \mathbf{X}_1 , \mathbf{V}_1 , and inputs $\mathbf{U}_{1:T-1}$, Algorithm 1 can be recursively applied to predict the trajectory $\hat{\mathbf{X}}_{2:T}$. Let ϕ denote the parameters of the GNN. The training objective is formulated as the following optimization problem:

$$\min_{\alpha, \phi} \sum_{t=1}^{T-1} \|\mathbf{X}_{t+1} - \hat{\mathbf{X}}_{t+1}\|_2 \quad (56)$$

Leveraging DEFT’s differentiability, T can be selected as greater than 2 to better capture long-term dynamics. This multi-step training approach results in improved prediction accuracy compared to single-step training, as demonstrated in Table 5.

Table 5: Ablation Study with Dataset 1

Method	Modeling Accuracy (RSME, 10^{-2} m) \downarrow Dataset 1	
	1	2
Single-step Training	2.22	3.41
Multi-step Training	1.87	2.82

C.3 Computational Speed

This section evaluates the computational efficiency of DEFT when compared to baseline methods. It also examines how employing the analytical gradient derived from Theorem 2 to compute (3) and the parallel programming approach detailed in Section 4.5, impacts overall computational time. All experiments in this section were conducted in Python on an Ubuntu 20.04 equipped with an AMD Ryzen PRO 5995WX CPU, 256GB of RAM, and 128 cores.

C.3.1 Computational Speed with Analytical Gradient

We compare the computational speed of using analytical gradients when compared to using numerical gradients. As summarized in Table 6, computing (3) with the analytical gradient is approximately twice as fast as using numerical gradients.

Table 6: Computational Time for (3) with Dataset 1

Method	Time (10^{-2} s)			
	1	2	3	4
Analytical Gradient	0.34	0.27	0.41	0.46
Numerical Gradient	0.74	0.65	0.84	0.91

C.3.2 Computational Speed with Parallel Programming

We compare the computational performance of using parallel programming approach described in Section 4.5 to a naive (sequential) implementation, in which each branch is simulated one after the other. In this experiment, we use the material properties of BDLO1 and gradually increase the number of children branches from 1 to 8. As shown in Figure 10, the naive implementation’s computation time grows more rapidly than that of the parallel approach. However, a certain increase in computational time is still expected with parallelization. As illustrated in Figure 6, constraints at each junction between the parent branch and its child branches prevent a fully batch-based operation, thereby resulting in an increase in the computational time.

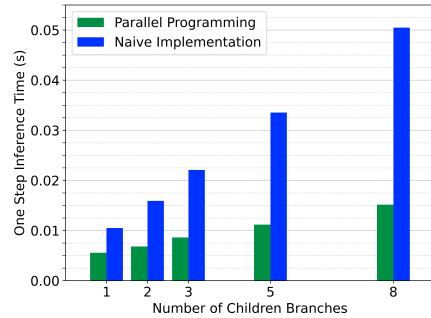


Figure 10: Computational speed comparison: parallel programming versus a naive (sequential) implementation.

C.4 Ablation Study on Residual Learning Architecture

To further demonstrate the significance of using GNN for residual learning, we replace it with the fully connected MLP described in Appendix B.3 and test on BDLO 2 and 3 from Dataset 1. We use BDLO 2 and 3 from dataset 1. As shown in Table 7, residual learning using a naive MLP is running slightly more efficient but provides limited improvements when compared to the proposed GNN approach. This illustrates the importance of the GNN because even modest improvements are important for prediction accuracy in long-term horizon predictions, where small errors can be significantly amplified during extended open-loop predictions.

Table 7: Ablation Study Comparing GNN and MLP Residual Learning Approaches

Method	Accuracy (10^{-2} m)		Comp. Time (10^{-2} s)	
	BDLO 2	BDLO 3	BDLO 2	BDLO 3
Replace GNN with MLP	3.11	1.64	0.67	0.72
DEFT	2.82	1.51	0.70	0.76

C.5 Modeling and Planning Visualization

Additional visulization of modeling and planning results can be found in Figure 11 and Figure 12 respectively.

D ARMOUR

To address the shape matching task, we employ ARMOUR [33], an optimization-based framework for motion planning and control. The objective is to guide a robot arm so that it manipulates a BDLO from an initial configuration to a specified target configuration. ARMOUR accomplishes this through a receding-horizon approach: at each iteration, it solves an optimization problem to determine the robot’s trajectory. ARMOUR parameterizes the robot’s joint trajectories as polynomials, with polynomial coefficients serving as the decision variables. One end of the rope is rigidly attached to the robot’s end effector, whose pose is determined by forward kinematics. By substituting the end effector’s final pose into DEFT, we obtain a prediction of the rope’s configuration at the conclusion of the motion. The optimization’s cost function then minimizes the Euclidean distance between this predicted BDLO configuration from DEFT and the target configuration. To ensure the resultant motion is physically feasible, ARMOUR incorporates constraints on the robot’s joint positions, velocities, and torques. Once the optimization is solved, the resulting trajectory is tracked by ARMOUR’s controller. This planning–execution process is repeated until the rope achieves the desired configuration or a maximum iteration threshold is exceeded (in which case the task is deemed a failure). Additional details on ARMOUR’s trajectory parameterization and its closed-loop controller can be found in [33, Section IX].

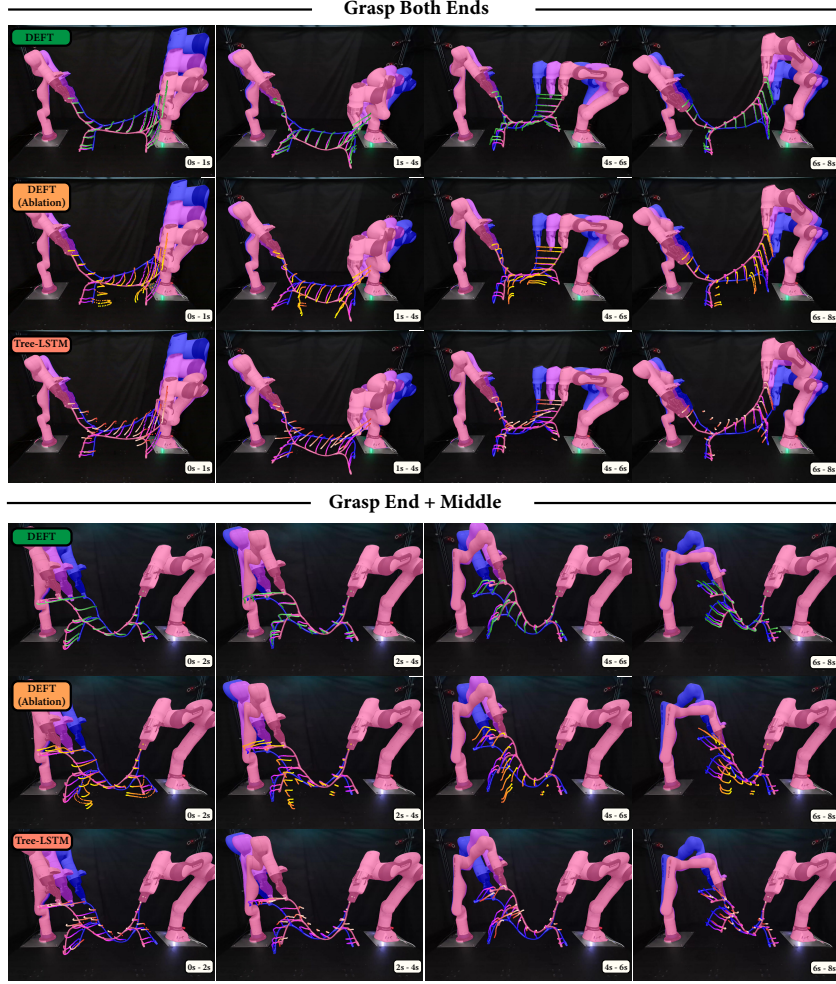


Figure 11: Visualization of the predicted trajectories for BDLO 1 under two manipulation scenarios, using DEFT, a DEFT ablation that leaves out the constraint described in Theorem 5, and Tree-LSTM. The ground-truth initial position of the vertices are colored in blue, the ground-truth final position of the vertices are colored in pink, and the gradient between these two colors is used to denote the ground truth location over time. The predicted vertices are colored as green circles (DEFT), orange circles (DEFT ablation), and light red circles (Tree-LSTM), respectively. A gradient is used for these predictions to depict the evolution of time, starting from dark and going to light. Note that the ground truth is only provided at $t=0s$ and prediction is constructed until $t=8s$. The prediction is performed recursively, without requiring additional ground-truth data or perception inputs throughout the entire process.

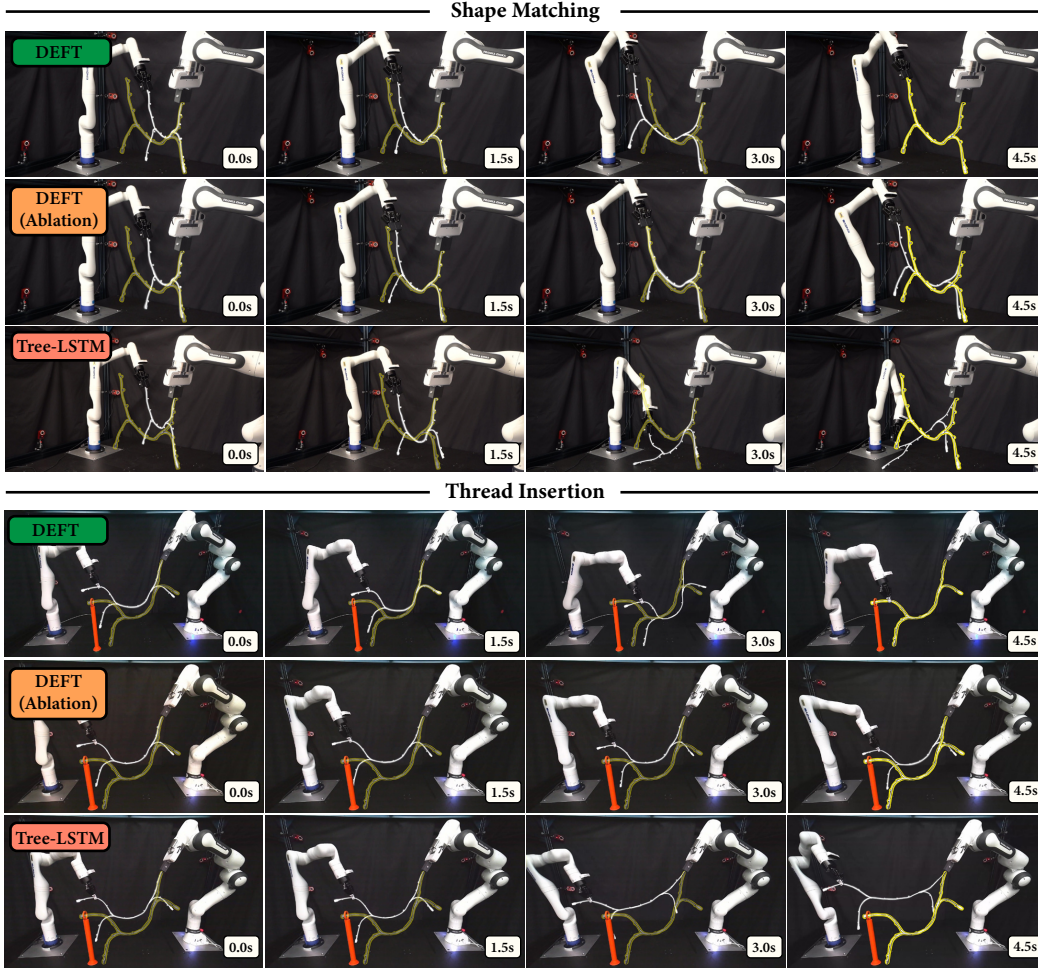


Figure 12: Visualization of planning for BDLO 1 for two manipulation tasks, using DEFT, a DEFT ablation that leaves out the constraint described in Theorem 5, and Tree-LSTM. The BDLO’s goal configuration is highlighted in yellow, while the target hole is shown in red. The DEFT model enables the planning algorithm to successfully complete the task, whereas the ablation approach of DEFT and the Tree-LSTM model both fail to finish tasks.